Resonance phenomena in a time-dependent, three-dimensional model of an idealized eddy

I. I. Rypina, L. J. Pratt, P. Wang, T. M. Özgökmen, and I. Mezic

Citation: Chaos: An Interdisciplinary Journal of Nonlinear Science **25**, 087401 (2015); doi: 10.1063/1.4916086
View online: http://dx.doi.org/10.1063/1.4916086
View Table of Contents: http://scitation.aip.org/content/aip/journal/chaos/25/8?ver=pdfcov
Published by the AIP Publishing

Resonance phenomena in a time-dependent, three-dimensional model of an idealized eddy

I. I. Rypina,[1] L. J. Pratt,[1] P. Wang,[2] T. M. Özgökmen,[2] and I. Mezic[3]
[1]*Woods Hole Oceanographic Institution, Woods Hole, Massachusetts 02543, USA*
[2]*Rosenstiel School of Marine and Atmospheric Science, University of Miami, Miami, Florida 33149, USA*
[3]*Department of Mechanical Engineering and Center for Control, Dynamical Systems and Computation, University of California, Santa Barbara, California 93106, USA*

(Received 3 October 2014; accepted 2 March 2015; published online 30 March 2015)

We analyze the geometry of Lagrangian motion and material barriers in a time-dependent, three-dimensional, Ekman-driven, rotating cylinder flow, which serves as an idealization for an isolated oceanic eddy and other overturning cells with cylindrical geometry in the ocean and atmosphere. The flow is forced at the top through an oscillating upper lid, and the response depends on the frequency and amplitude of lid oscillations. In particular, the Lagrangian geometry changes near the resonant tori of the unforced flow, whose frequencies are rationally related to the forcing frequencies. Multi-scale analytical expansions are used to simplify the flow in the vicinity of resonant trajectories and to investigate the resonant flow geometries. The resonance condition and scaling can be motivated by simple physical argument. The theoretically predicted flow geometries near resonant trajectories have then been confirmed through numerical simulations in a phenomenological model and in a full solution of the Navier-Stokes equations. © *2015 AIP Publishing LLC*. [http://dx.doi.org/10.1063/1.4916086]

Resonance phenomena, where a system's response is enhanced for certain forcing frequencies, arise in a variety of different scientific disciplines from biology to plasma physics. In geophysical fluid flows, resonances can alter the geometry of Lagrangian motion, produce or destroy transport barriers, and thus modify some of the key oceanographic properties of the flow such as the ability of the system to redistribute tracers and mix water masses. In this paper, we explore these ideas in application to an oceanic eddy. Oceanic eddies help maintain the large-scale hydrographic structure, stratification, general circulation, and distribution of bio and geo-chemical tracers throughout the World Oceans. Yet, the geometry of Lagrangian motions and material barriers that exist within an eddy, the exact mechanism by which eddies trap and shape the tracer fields, as well as their response to changing wind forcing are not totally understood. Our work provides a piece of a puzzle by exploring the Lagrangian geometry and investigating transport barriers in an idealized model of an isolated oceanic eddy.

I. INTRODUCTION

Fluid flows that combine a horizontal swirling motion with vertical overturning occur in hurricanes, ocean mesoscale eddies, and many industrial applications involving laminar mixing technologies. Relevant industrial flows include, for example, flows inside a lid-driven cylindrical cavity or rotating sphere (Znaien *et al.*, 2012; Pouransari *et al.*, 2010; and Moharana *et al.*, 2013). A classical model for ocean applications is the "rotating can" flow (Fig. 1), in which fluid is confined within a rigid rotating cylinder with solid vertical walls and top/bottom lids. Different versions of this flow can be driven thermally by heating/cooling of the bottom/top, or by boundary stresses at the top/bottom surface induced, for example, by rotating the lid at a slightly different speed compared to the cylinder walls. Either mechanism will generate vertical overturning in addition to the azimuthal rotation. Both buoyancy and surface stress forcings can occur naturally in oceanic flows due to the heat exchange with the atmosphere and wind stresses, making the "rotating can" flow a suitable, although highly idealyzed, model for studying certain aspects of oceanic eddies. The Eulerian velocity field produced in the "rotating can" setting, and in variations thereof, has been the subject of numerous investigations (e.g., Lopez and Marques, 2010 and references contained therein) and is a central focus of Greenspan's Theory of Rotating Fluids (Greenspan, 1968). On the other hand, attention to Lagrangian aspects of the flow fields, including chaotic advection, Lagrangian transport barriers, and implications for stirring and mixing, has been relatively limited. The main topic of the current study is the geometry of Lagrangian motion and material barriers in a time-dependent rotating can flow driven by the surface stress at the upper surface.

The circulation in ocean eddies differs from that of the homogeneous rotating can in many respects. An isolated ocean eddy typically has an azimuthal velocity field that decays away from the center and lies sufficiently far from neighboring eddies as to be only weakly influenced by them. In the rotating can, the circulation is laterally confined by rigid cylinder wall, a common artifice used in idealized models to limit the computational domain. Although real eddies are influenced by surface winds, which can cause upwelling and downwelling (e.g., McGillicuddy *et al.*, 2007; Ledwell *et al.*, 2008), they are often generated by

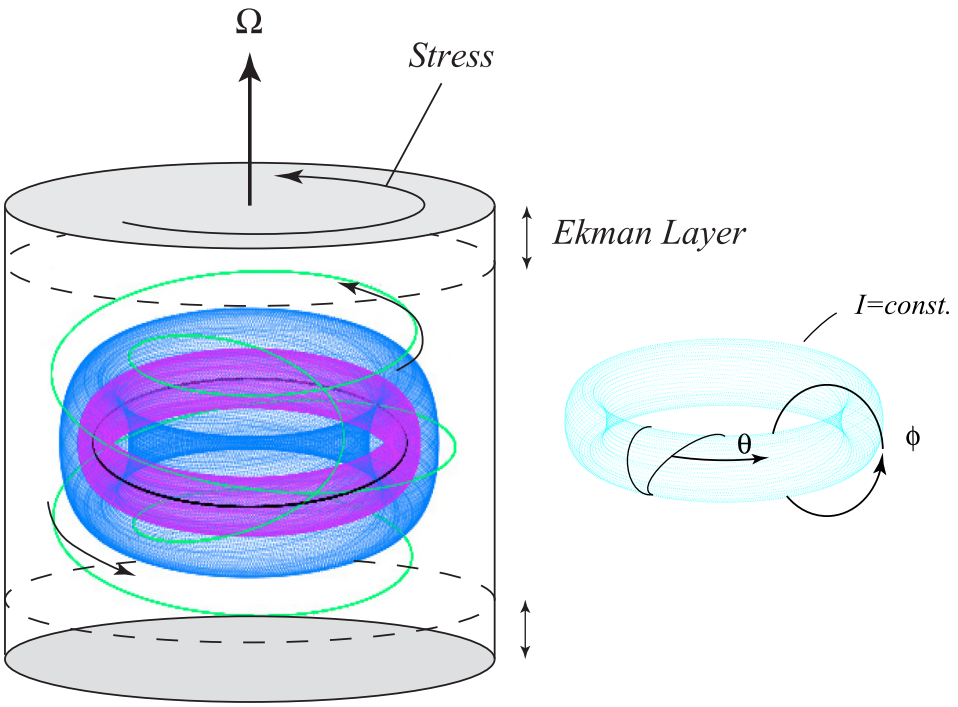

FIG. 1. (left) Schematic diagram showing the Lagrangian geometry of a steady axisymmetric rotating can flow. The surfaces traced out by four trajectories are shown with different colours. Blue and purple surfaces are associated with quasiperiodic trajectories; green and black correspond to periodic trajectories. (right) Action-angle-angle variables (I, θ, ϕ).

hydrodynamic instability and not directly by the wind stress. In the rotating can, all motion seen in the rotating frame is forced by the surface wind stress. Other neglected influences of potential oceanographic importance include small scale turbulence and density stratification, neither of which is present in the rotating can model for a homogeneous flu id at moderate Reynolds number. Despite these limitations, the 3D circulation in the rotating can has the generic elements of isolated ocean features with horizontal swirl and vertical overturning, one reason that it has become a canonical model fluid dynamics and the subject of hundreds of research papers.

Chaotic advection in a three-dimensional cylinder flow was studied by Fountain *et al.* (2000) for the case of steady flow at low Reynolds numbers. The flow was driven near the top by an impellor that can be tilted relative to the cylinder axis. Background rotation was zero for most cases. When the impeller tilt is zero, an axisymmetric flow is produced, with upwelling in the interior, downwelling at the outer edges, and an overall horizontal swirling. The independence of this circulation on the azimuthal coordinate implies that for the overturning flow, a transport stream function with closed contours can be defined in the vertical (r, z)-plane, and this implies that all fluid trajectories are confined to tori. Some tori have quasiperiodic trajectories that never come back to their exact starting point (these are illustrated by blue and purple surfaces in Figure 1, although the details of our rotating can model differ from the one considered by Fountain *et al.* (2000)), while others have periodic trajectories (illustrated by the green curve) that come back to their starting point after each complete period of motion. If the impellor is tilted, axial symmetry is broken and the tori with periodic orbits become resonant. Chaotic trajectories are produced in the vicinity along with new invariant tori. The latter resemble twisted hulu hoops and are visualized by Fountain *et al.* (2000) using dye injection in a laboratory model. As predicted by Cheng and Sun (1990); Xia (1992); and Mezic and Wiggins (1994), some of the non-resonant tori survive the symmetry breaking perturbation.

Pratt *et al.* (2014) considered a similar rotating can flow, but with oceanographically important strong background rotation induced by the fast rotation of the vertical cylinder walls and bottom lid, and an imposed stress at the top surface induced by a slightly different rotational speed of the top lid compared to the walls. In the oceanographic context, this surface stress could be due, for example, to wind forcing. The velocity fields are generated by high-resolution numerical integration of the Navier-Stokes equations, and a range of oceanograpically relevant Ekman and Rossby numbers (*Ek* and *Ro*) is considered. For the rotating can flow, these two dimensionless parameters completely describe the parameter space of the system, and the Reynolds number can be expressed through *Ek* and *Ro*. Generally speaking, Ekman layers are generated at the top and bottom of the tank. If the stress at the top surface is cyclonic, i.e., the top lid rotates faster than the walls, the upper Ekman layer is divergent and fluid is sucked up from the interior, and spun out to the outer part of the cylinder, where it descends into a convergent bottom Ekman layer and is returned up into the interior. There is also a cyclonic azimuthal flow. When the surface stress is purely azimuthal and axisymmetric, it is easy to show, again, that all trajectories live on tori. When the imposed surface stress is asymmetric, chaos is generated by the resonant breakup of tori. The authors also used tracer release experiments to quantify the overall stirring rate and show that it is significantly enhanced by Lagrangian chaos.

Another mechanism by which chaos can be induced into the system by the asymmetric surface stress is through the breakup of the heteroclinic central streamline (which in the axisymmetric steady background flow connects the

hyperbolic stagnation point at the bottom to the hyperbolic stagnation point at the top) into one-dimensional stable and unstable manifolds (1D curves in 3D space). In 2D fluid flows, such 1D stable and unstable manifolds would repeatedly intersect each other, creating closed areas of fluid called lobes, and facilitating chaotic advection via the lobe dynamics mechanism (Rom-Kedar *et al.*, 1993; Samelson and Wiggins, 2006; and Rypina *et al.*, 2010, 2011). In our 3D flow, the role of 1D stable and unstable manifolds is less clear as they cannot form lobes in 3D and thus cannot drive the lobe dynamics. Associated with the hyperbolic stagnation points at the top and bottom of the cylinder, there are also 2D stable and unstable manifolds (Mireles-James and Lomeli, 2010; Lomeli and Ramirez-Ros, 2008). In the rotating can flow, which is confined within the rigid cylinder walls, these manifolds coincide with each other and with the outer cylinder walls in both the axisymmetric background and the non-symmetric perturbed flow. If the flow was not constrained by the presence of the rigid outer walls and was allowed to interact with other eddies, the symmetry-breaking disturbance could lead to the breakup of the outer boundary of the eddy into two-dimensional stable and unstable manifolds (2D surfaces in 3D space), which would intersect each other, form lobes, and facilitate chaotic exchange of fluid between the interior and exterior of the cylinder via the lobe dynamics. This mechanism is prohibited, however, in our system due to the presence of the rigid cylindrical walls.

In a different version of the cylinder problem, Lackey and Sotiropoulos (2006) consider the rotating can flow case in which the bottom lid rotates in the opposite direction to the top lid, and there is no rotation of the vertical cylinder walls. This forcing results in the formation of separate, counter-rotating cells at the top and bottom of the cylinder. A steady perturbation can induce resonances within tori belonging to either of the cells, and chaotic transport between the cells.

Each of these investigations is confined to steady perturbations of a steady background flow. In order to "nudge" this body of work closer to ocean and atmospheric reality, we now consider the case of time-dependent perturbations. We will largely limit our discussion to time-periodic and quasi-periodic disturbances, and will focus on the generation of chaos through the resonant breakup of tori.

The results reported here differ from those obtained from a widely-used, kinematic model of side-by-side convection cells (Solomon and Mezic, 2003, and also see Vainchtein *et al.*, 2007, 2008), which is more complex in some respects and simpler in others. In the "Solomon vortex chain," neighboring cells are in physical contact and are allowed, under perturbation, to exchange fluid with each other, a feature prevented by our rigid cylinder walls. On the other hand, vertical motion is present in the perturbation and not the basic state, so that there are two slow and one fast variable (action-action-angle coordinates), similar to the case considered by Cartwright *et al.* (1995, 1996). In our case, vertical motion is present in the undisturbed state and the system is best described by action-angle-angle coordinates that provide a natural reference frame for our flow.

In Sec. II, we describe in more detail our version of the rotating can flow, along with the phenomenological equations and full numerical model for the velocity fields. Then in Sec. III, we formalize and extend the ideas of Zaslavsky and Chirikov (1972); Zaslavsky (1985); and Rypina *et al.* (2007a) to our 3D, time-dependent flow, and investigate the behavior of the system in the vicinity of resonant tori using multi-scale expansions that are carried out in terms of action-angle-angle variables. The disturbance in our analysis is decomposed into a set of waves that propagate around the resonant torus in question. Conditions for resonance agree with those found by Dullin and Meiss (2012) through a different argument. Our analysis yields to an approximate analytical description of the flow near resonant tori, allowing for investigating the geometries of Lagrangian motion within resonant layers (Sec. IV). These theoretically-predicted geometries are then tested numerically in Sec. V by producing resonances in the phenomenological model of the rotating can flow and in the full numerical solution obtained by solving the Navier-Stokes equations. Throughout the discussion, we attempt to illustrate and portray the geometry of Lagrangian motion and transport barriers in Cartesian (x, y, z) space using single and double stroboscopic sections, where particle trajectory is strobed in time after each period of the perturbation and then in azimuthal angle after completing each full cycle in azimuth. Structures that are straightforward to visualize in action-angle-angle space become twisted and folded in the (x, y, z) space, and can be challenging to visualize. In addition, clear-cut visualizations using double stroboscopic sections in the Navier-Stokes simulation are numerically challenging due to the necessity of integration over tens of thousands of cycles. We therefore add a tracer release experiment to provide an alternative visualization and to verify that dye is confined by the barrier in the way anticipated from the theory.

II. ROTATING CAN FLOW

A. Flow geometry

The fluid flow that we are considering arises in a rotating cylinder with solid walls and top/bottom lids, whose top lid rotates at a slightly different angular speed. The curl of the surface stress leads to a divergence in the surface Ekman layer and induced upwelling or downwelling. The resulting circulation consists of both azimuthal swirling and vertical overturning. For lid rotation slightly faster than that of the cylinder, trajectories spiral up around the cylinder axis, then spiral to the outside perimeter in the top boundary layer, then spiral down within the wall boundary layer, and finally spiral back towards the center near the bottom, so the cycle can be repeated again. In the steady axisymmetric background state, all trajectories lie on tori. As asymmetry and time-dependence are introduced into the system through, for example, off-center shift and oscillatory motion of the top lid, some of the tori break down due to the excitation of resonances, and chaotic motion becomes possible.

B. Phenomenological model and full numerical solution of the Navier–Stokes equations

A phenomenological model has been introduced in Pratt *et al.* (2014) that describes all of the qualitative features of this flow. Here, we use a similar phenomenological model as well as a fully nonlinear numerical solution of the Navier-Stokes equations to construct examples of resonances and visualize the flow geometry within resonant layers. Specifically, the phenomenological velocities are given by

$$\begin{aligned} u &= -bx(1-2z)\frac{R-r}{3} - ay(c+z^2) \\ &\quad + \epsilon\left[y(y-y_0+\gamma\cos(\sigma t)) - \frac{R^2-r^2}{2}\right](1-\beta z), \qquad (1) \\ v &= -by(1-2z)\frac{R-r}{3} + ax(c+z^2) \\ &\quad - \epsilon x(y-y_0+\gamma\cos(\sigma t))(1-\beta z), \\ w &= bz(1-z)\left(\frac{2R}{3}-r\right), \end{aligned}$$

with $r=\sqrt{x^2+y^2}$, forcing period $T_f=2\pi/\sigma$, and parameter values $R=0.5$ (cylinder radius), $a=0.62$ (strength of azimuthal rotation), $b=7.5$ (strength of vertical overturning), $c=0.7$ (the term $(c+z^2)$ introduces deviation from the solid-body rotation), $\beta=1$ (strength of depth dependence), $\gamma=0.2$ (strength of time-dependence), and $y_0=-0.2$ (shift of the upper lid). The velocity field described by (1) is incompressible (volume conserving) and satisfies the condition of no-normal-flow at all solid boundaries. The $O(1)$-terms in the right-hand side of (1) define the background flow and $O(\epsilon)$-terms represent the perturbation. The perturbation can be made multi-periodic by introducing more frequency components, but here, we use periodic forcing with only one σ.

The fully numerical solution of the Navier-Stokes equations was obtained using the spectral element model Nek5000 (http:nek5000.mcs.anl.gov/index.php/Main_Page) developed by Fischer and colleagues (Patera, 1984; Maday and Patera, 1989; and Fischer, 1997). All system parameters ($Ek=1/50$, $Ro=0.2$, $Re=10$, cylinder radius $R=1$ and cylinder height $H=1$) in our simulations are identical to those used to produce Fig. 10(i) in Pratt *et al.* (2014). However, instead of imposing a steady shift of the upper lid as in that paper, here we impose a periodic oscillation of the upper lid around its shifted position. The horizontal velocity imposed at the upper lid is given by

$$u=-4y(1-r), \quad v=4(x-x_0)(1-r), \qquad (2)$$

where $r=\sqrt{x^2+y^2}$ and $x_0=X_0+dX\cos\sigma t$, where $\sigma=2\pi/T_f$ is the forcing frequency, $X_0=-0.007$, and $dX=0.005$.

III. RESONANCES

Cheng and Sun (1990) and Xia (1992) showed that some tori will survive a small-amplitude, time-periodic perturbation of the axisymmetric, volume preserving flow that we are considering. The surviving tori are non-resonant in some sense, though there is no established method for identification of the tori that survive. Fox and Meiss (2013) used Greene's residue criterion to predict the destruction of tori and to identify the most robust torus, and Meiss (2012) investigated the critical perturbation strength and the breakup of the last invariant torus in a three-dimensional generalized standard map. We will concentrate instead on the conditions for resonance, and the consequences for the dynamics in the vicinity of a resonant torus. Our analysis will be carried out in the action-angle-angle coordinates defined by Mezic and Wiggins (1994). As shown in Figure 1, the action variable I is a label for an undisturbed torus, while θ and ϕ are angles that wrap around the tori in the azimuthal and meridional directions. The angle variables are defined such that the angular velocities are constants of motion, denoted Ω_θ and Ω_ϕ, respectively. The angle coordinates therefore depend on the properties of trajectories on the undisturbed tori and the general transformations are given by Mezic and Wiggins (1994).

We now consider a perturbation of amplitude ϵ, $\epsilon \ll 1$, to the undisturbed velocity field. The trajectory equations can then be written in the action-angle-angle variable set as

$$\begin{aligned} \dot{I} &= \epsilon F^0(I,\phi,\theta,\vec{\sigma}t), \qquad (3) \\ \dot{\phi} &= \Omega_\phi(I) + \epsilon F^1(I,\phi,\theta,\vec{\sigma}t), \\ \dot{\theta} &= \Omega_\theta(I) + \epsilon F^2(I,\phi,\theta,\vec{\sigma}t), \end{aligned}$$

where I is the action variable, ϕ and θ are the two angle variables, and the perturbation is quasi-periodic in time with frequencies $\vec{\sigma}=\{\sigma_1,\ldots,\sigma_n\}$. Without loss of generality, the frequency components σ_i can be assumed to be incommensurate, otherwise frequency reduction will be possible.

The perturbation fields may be expanded in Fourier series as

$$\begin{aligned} (F^0,F^1,F^2) &= \sum_{n,m,l_1,l_2,\ldots=-\infty}^{\infty}\left(F^0_{nml\vec{}}(I),F^1_{nml\vec{}}(I),F^2_{nml\vec{}}(I)\right) \\ &\quad \times \sin\left(n\phi+m\theta-\vec{l}\cdot\vec{\sigma}t+\alpha_{nml\vec{}}\right), \qquad (4) \end{aligned}$$

where n, m, and $\vec{l}=\{l_1,\ldots,l_n\}$ are integers and $\alpha_{nml\vec{}}$ are phases.

In the remainder of this section, we discuss the conditions for resonance for our 3D system, and we map out the structures that arise in an isolated resonant layer. The discussion begins in Subsection III A with physical interpretation of the phenomenon of resonance, leading to an intuitive picture of the processes occurring near a resonant torus. This discussion also suggests relevant time and amplitude scales (Subsection III B), which are then used to motivate a more formal development (Subsection III C) based on a multiple-scale expansion. The geometry of the solution depends on the number of independent resonant disturbances, and this is dealt with in Subsection III D.

A. Resonances: Physical meaning

Note that each sin term in Eq. (4) consists of a progressive wave that sweeps around the undisturbed tori. Each such wave has quantized wave numbers n and m, and

frequency $\vec{l}\cdot\vec{\sigma}$. The lines of constant phase are perpendicular to the unit normal $\vec{n}=(n,m)/(n^2+m^2)^{1/2}$, and the wave propagates in the normal direction with the speed $c_{nml}=\vec{l}\cdot\vec{\sigma}/(n^2+m^2)^{1/2}$. These features are portrayed in Fig. 2(a) in the periodic (ϕ,θ)-plane, which can be thought of as the flattened surface of a particular undisturbed torus $I=I_0$.

If the flow is only weakly disturbed, a fluid element starting at $I=I_0$ has an angular velocity very close to that of the undisturbed flow: $\vec{c}_p=(\Omega_\phi(I_0),\Omega_\theta(I_0))$. This velocity is indicated by an arrow in Figure 2(a). If the component $\vec{c}_p\cdot\vec{n}$ of this velocity normal to the phase lines matches the disturbance phase speed c_{nml}, then the fluid element remains attached to a line of constant phase of the disturbance, and resonance will occur. Use of the previous expressions for c_{nml}, $\vec{n}$, and $\vec{c}_p$ yield the resonance condition

$$n\Omega_\phi(I_0)+m\Omega_\theta(I_0)-\vec{l}\cdot\vec{\sigma}=0. \tag{5}$$

Because of the phase locking, the contribution $\epsilon F^0_{nml}(I_0)\sin(n\phi+m\theta-\vec{l}\cdot\vec{\sigma}t+\alpha_{nml})$ to the velocity of the element normal to the torus will remain constant along the fluid trajectory, and the later will move steadily away from the torus I_0, inward or outward depending on the phase. Trajectories which happen to follow phase lines with phase 0 or π will experience no normal displacement due to the resonant term. The trajectories are also potentially influenced by other resonant forcing terms, and, to a smaller extent, by non-resonant terms that are not phase locked with the fluid parcel and whose phase oscillates in sign.

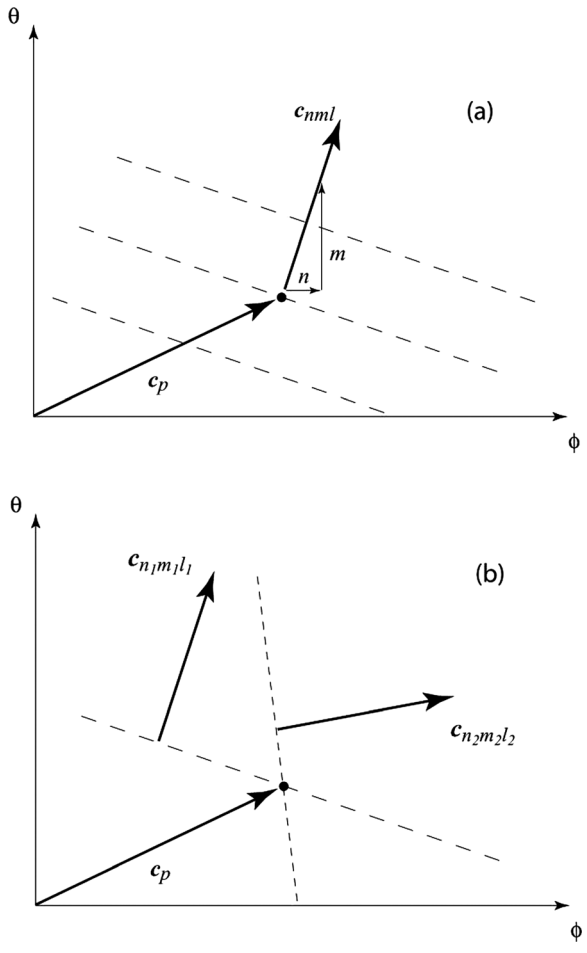

FIG. 2. Schematic diagram of the resonance in terms of plane waves.

Note that if the forcing is steady ($\sigma=0$), then the lines of constant phase are fixed and the condition for resonance is that the parcel trajectory follows one of these fixed lines. Since the disturbance is periodic in θ and ϕ, the lines of constant phase must eventually close as they wrap around the torus, and thus, the trajectory must also be periodic. Therefore, as noted in Pratt *et al.* (2014), resonances under steady forcing can only occur for tori with periodic trajectories.

B. Resonances: Scaling

Since the velocity normal to the torus is initially $O(\epsilon)$, the separation $\delta I=I-I_0$ of a trajectory from a resonant torus increases in proportion to ϵt. As the trajectory moves away from I_0 and onto a new undisturbed torus $I_0+\delta I$, its angular velocity will generally change. To a first approximation, the new angular speeds are those of the undisturbed flow at the new value of I, namely $\Omega_\phi(I_0+\delta I)$ and $\Omega_\theta(I_0+\delta I)$. At the same time, the frequency $\vec{l}\cdot\vec{\sigma}$ of the resonant disturbance remains unchanged, so resonance is generally lost. In fact, the resonance condition (5) applied at $I_0+\delta I$ is

$$\begin{aligned} &n\Omega_\phi(I_0+\delta I)+m\Omega_\theta(I_0+\delta_I)-\vec{l}\cdot\vec{\sigma}\\ &\quad\approx\delta I\left(n\frac{d\Omega_\phi}{dI}+m\frac{d\Omega_\theta}{dI}\right)_{I=I_0}=0; \end{aligned} \tag{6}$$

so, unless $\left(n\frac{d\Omega_\phi}{dI}+m\frac{d\Omega_\theta}{dI}\right)_{I=I_0}=0$, the resonance condition for the trajectory is violated by an amount proportional to $\delta I\sim\epsilon t$. Recall that the left-hand side of Eq. (6) is proportional to the difference between the phase speed of the disturbance and the normal component of the trajectory velocity, so that the difference between the *phase* of the disturbance and the trajectory grows in proportion to ϵt^2. Thus, a trajectory that is phase locked to the disturbance at $t=0$ experiences a phase change of order $\pi/2$ over a time period of $O(\epsilon^{-1/2})$, at which point the sign of the normal velocity $\delta\dot{I}$ will reverse. Over this time period, δI will have grown to $O(\epsilon^{1/2})$. These arguments and scalings are similar to what is found in nonlinear critical levels for waves in shear flows (e.g., Maslowe and Clarke, 2002).

It is also possible that the terms involving the first derivatives of Ω_ϕ and Ω_θ with respect to I in Eq. (6) may vanish, meaning that, to the lowest order, the trajectory remains phase locked to the disturbance as it drifts away from the torus I_0. In this case, the Taylor expansion of $n\Omega_\phi(I_0+\delta I)+m\Omega_\theta(I_0+\delta I)$ must be carried out to the first nonzero (j-th) derivative, $\frac{d^j(n\Omega_\phi+m\Omega_\theta)}{dI_j}|_{I=I_0}$. j is often referred to as the order of degeneracy, and $j=1$ corresponds to the non-degenerate case. The term on the right of Eq. (6) now becomes $O(\delta I)^j$ and grows in proportion to $(\epsilon t)^j$. The phase difference between the trajectory and the disturbance therefore grows in proportion to $\int(\epsilon t)^j dt=\epsilon^j t^{j+1}$, and resonance is lost over $t\sim O(\epsilon^{-j/(j+1)})$. At this stage, δI has grown to $O(\epsilon^{1/(j+1)})$.

C. Multiple-scale analysis near resonant tori

The most common case of resonance will be non-degenerate (i.e., $j=1$), and we now formalize the preceding phenomenological discussion through the use of a multiple-scale analysis. The procedure for degenerate cases ($j>1$) is similar and appears in Appendix A. For $j=1$, we anticipate that δI will grow to $O(\epsilon^{1/2})$ over a time of $O(\epsilon^{-1/2})$, suggesting the expansions

$$\begin{aligned}\delta I &= \epsilon^{1/2}\delta I_0(t,\tau)+\epsilon\delta I_1(t,\tau)+\cdots\\ \phi &= \phi_0(t,\tau)+\epsilon^{1/2}\phi_1(t,\tau)+\cdots\\ \theta &= \theta_0(t,\tau)+\epsilon^{1/2}\theta_1(t,\tau)+\cdots,\end{aligned}$$

where $\tau=\epsilon^{1/2}t$.

By the standard procedure for multiple-scale analysis, we substitute the expansions into Eq. (3), treating t and τ as independent variables, and replacing time derivatives by $\frac{d}{dt}=\frac{\partial}{\partial t}+\epsilon^{1/2}\frac{\partial}{\partial\tau}$. The equations for δI, θ, and ϕ then become

$$\begin{aligned}&\epsilon^{1/2}\frac{\partial}{\partial t}\delta I_0+\epsilon\frac{\partial}{\partial\tau}\delta I_0+\epsilon\frac{\partial}{\partial t}\delta I_1+\cdots\\ &\quad=\epsilon\sum_{nm\vec{l}}F^0_{nm\vec{l}}\left(I_0+\epsilon^{1/2}\delta I_0+\cdots\right)\sin\left[n\left(\phi_0+\epsilon^{1/2}\phi_1+\cdots\right)\right.\\ &\qquad\left.+m\left(\theta_0+\epsilon^{1/2}\theta_1+\cdots\right)-\vec{l}\cdot\vec{\sigma}t+\alpha_{nm\vec{l}}\right]\end{aligned}\tag{7}$$

and

$$\begin{aligned}&\frac{\partial}{\partial t}\phi_0+\epsilon^{1/2}\frac{\partial}{\partial\tau}\phi_0+\epsilon^{1/2}\frac{\partial}{\partial t}\phi_1+\cdots\\ &\quad=\Omega_\phi\left(I_0+\epsilon^{1/2}\delta I_0+\cdots\right)+\epsilon\sum_{nm\vec{l}}F^1_{nm\vec{l}}\left(I_0+\epsilon^{1/2}\delta I_0+\cdots\right)\\ &\qquad\times\sin\left[n\left(\phi_0+\epsilon^{1/2}\phi_1+\cdots\right)+m\left(\theta_0+\epsilon^{1/2}\theta_1+\cdots\right)\right.\\ &\qquad\left.-\vec{l}\cdot\vec{\sigma}t+\alpha_{nm\vec{l}}\right]\end{aligned}\tag{8}$$

with a similar equation for θ.

The lowest order approximation just describes motion of the undisturbed flow

$$\frac{\partial\delta I_0}{\partial t}=0;\quad \frac{\partial\theta_0}{\partial t}=\Omega_\theta(I_0);\quad \frac{\partial\phi_0}{\partial t}=\Omega_\phi(I_0).$$

Therefore

$$\begin{aligned}\delta I_0&=\delta\tilde{I}_0(\tau),\\ \phi_0&=\Omega_\phi(I_0)t+\tilde{\phi}_0(\tau),\\ \theta_0&=\Omega_\theta(I_0)t+\tilde{\theta}_0(\tau).\end{aligned}\tag{9}$$

Note that $\delta\tilde{I}_0(0)$, $\tilde{\phi}_0(0)$, and $\tilde{\theta}_0(0)$ are set by the initial conditions on δI, θ, and ϕ, which determine the trajectory one wishes to compute.

At next order, we have

$$\begin{aligned}\frac{\partial}{\partial t}\delta I_1=&-\frac{\partial}{\partial\tau}\delta\tilde{I}_0+\sum_{nm\vec{l}}F^0_{nm\vec{l}}(I_0)\sin\left[\tilde{\eta}_{nm\vec{l}}(\tau)\right.\\ &\left.+(n\Omega_\phi(I_0)+m\Omega_\theta(I_0)-\vec{l}\cdot\vec{\sigma})t\right],\end{aligned}\tag{10a}$$

$$\frac{\partial\phi_1}{\partial t}=-\frac{\partial\tilde{\phi}_0}{\partial\tau}+\left(\frac{d\Omega_\phi}{dI}\right)_{I_0}\delta\tilde{I}_0,\tag{10b}$$

$$\frac{\partial\theta_1}{\partial t}=-\frac{\partial\tilde{\theta}_0}{\partial\tau}+\left(\frac{d\Omega_\theta}{dI}\right)_{I_0}\delta\tilde{I}_0,\tag{10c}$$

where the slowly-varying part of the phase function is $\tilde{\eta}_{nm\vec{l}}=n\tilde{\phi}_0(\tau)+n\tilde{\theta}_0(\tau)+\alpha_{nm\vec{l}}$. The terms on the right-hand sides of Eqs. (10b) and (10c) are independent of t, and thus, the solutions for ϕ_1 and θ_1 will grow linearly in t. The asymptotic expansion would then become invalid after a time $t\sim O(\epsilon^{-1/2})$. To prevent this secular growth, we must set the right-hand side terms to zero, and thus

$$\frac{\partial\tilde{\phi}_0}{\partial\tau}=\left(\frac{d\Omega_\phi}{dI}\right)_{I_0}\delta\tilde{I}_0,\tag{11a}$$

$$\frac{\partial\tilde{\theta}_0}{\partial\tau}=\left(\frac{d\Omega_\theta}{dI}\right)_{I_0}\delta\tilde{I}_0,\tag{11b}$$

or

$$\frac{\partial\tilde{\eta}_{nm\vec{l}}}{\partial\tau}=\left(n\frac{d\Omega_\phi}{dI}+m\frac{d\Omega_\theta}{dI}\right)_{I_0}\delta\tilde{I}_0.\tag{12}$$

The first term on the right-hand side of Eq. (10a) is independent of t, and any member of the second group of terms will also be t-independent, provided that $n\Omega_\phi(I_0)+m\Omega_\theta(I_0)\ -\vec{l}\cdot\vec{\sigma}=0$, which is the previously identified resonance condition (5). To prevent secular growth of δI_1, we must have

$$\frac{\partial}{\partial\tau}\delta\tilde{I}_0=\sum_{nm\vec{l}}^{resonant}F^0_{nm\vec{l}}(I_0)\sin\left(\tilde{\eta}_{nm\vec{l}}\right).\tag{13}$$

We note that (12) and (13) have the following integral of motion with respect to the slow time variable

$$G\left(\delta\tilde{I}_0,\tilde{\eta}_{n_1m_1\vec{l}_1},\tilde{\eta}_{n_2m_2\vec{l}_2},\ldots\right)=\frac{\delta\tilde{I}_0^2}{2}+\sum_{nm\vec{l}}^{resonant}\frac{F^0_{nm\vec{l}}(I_0)\cos\left(\tilde{\eta}_{nm\vec{l}}\right)}{\left.\frac{d(n\Omega_\phi+m\Omega_\theta)}{dI}\right|_{I_0}}.\tag{14}$$

Note that there are at most two linearly-independent coordinates $\tilde{\eta}_{nm\vec{l}}$; that is, if we define the two coordinates $\tilde{\eta}_{n_1m_1\vec{l}_1}=n_1\tilde{\phi}_0(\tau)+m_1\tilde{\theta}_0(\tau)+\alpha_{n_1m_1\vec{l}_1}$ and $\tilde{\eta}_{n_2m_2\vec{l}_2}=n_2\tilde{\phi}_0(\tau)+m_2\tilde{\theta}_0(\tau)+\alpha_{n_2m_2\vec{l}_2}$ such that (n_2, m_2) is not an integer multiple of (n_1, m_1), then any other coordinate $\tilde{\eta}_{n_3m_3\vec{l}_3}=n_3\tilde{\phi}_0(\tau)+m_3\tilde{\theta}_0(\tau)+\alpha_{n_3m_3\vec{l}_3}$ can always be expressed through a linear combination of the first two coordinates with constant coefficients A, B, and C: $\tilde{\eta}_{n_3m_3\vec{l}_3}=A\tilde{\eta}_{n_1m_1\vec{l}_1}+B\tilde{\eta}_{n_2m_2\vec{l}_2}+C$. Thus, G is most generally defined on the three dimensional space $[\delta\tilde{I}_0(\tau),\tilde{\eta}_{n_1m_1\vec{l}_1}(\tau),\tilde{\eta}_{n_2m_2\vec{l}_2}(\tau)]$ or, equivalently, $[\delta\tilde{I}_0(\tau),\tilde{\phi}_0(\tau),\tilde{\theta}_0(\tau)]$.

For further interpretation, we consider the expansion terms computed thus far

$$\delta I(t,\tau) = \epsilon^{\frac{1}{2}}\tilde{\delta I}_0(\tau) + \epsilon\left[\tilde{\delta I}_1(\tau) - \sum_{nml}^{nonres}\frac{F^0_{nml}(I_0)}{r_{nml}(I_0)} \times \cos\left(\tilde{\eta}_{nml}(\tau) + r_{nml}(I_0)t\right)\right] + O\left(\epsilon^{\frac{3}{2}}\right), \quad (15a)$$

$$\phi = \Omega_\phi(I_0)t + \tilde{\phi}_0(\tau) + \epsilon^{\frac{1}{2}}\tilde{\phi}_1(\tau) + O(\epsilon), \quad (15b)$$

$$\theta = \Omega_\theta(I_0)t + \tilde{\theta}_0(\tau) + \epsilon^{\frac{1}{2}}\tilde{\theta}_1(\tau) + O(\epsilon), \quad (15c)$$

where $r_{nml}(I_0) = n\Omega_\phi(I_0) + m\Omega_\theta(I_0) - \vec{l}\cdot\sigma$. At lowest order, it can be seen that fluid elements rapidly sweep around the unperturbed torus with the angular speeds Ω_ϕ and Ω_θ, and slowly execute displacements $\epsilon^{1/2}\tilde{\delta I}_0(\tau)$, $\tilde{\phi}_0(\tau)$, and $\tilde{\theta}_0(\tau)$ relative to the unperturbed motion. An observer moving in a frame of reference following the unperturbed motion will observe fluid elements moving along the level surfaces of the function G. Since G does not depend explicitly on τ, the surfaces remain fixed in the moving frame.

We have also included in (15) the non-resonant contributions to the solutions to (10) which, in the case of (10b) and (10c), are just undetermined functions $\tilde{\phi}_1(\tau)$ and $\tilde{\theta}_1(\tau)$ of the slow variable. The nonresonant solution to (10a) is the sum of a slowly varying function $\tilde{\delta I}_1(\tau)$ and a set of rapidly-varying oscillations. All of these terms are of higher order and will largely be disregarded in subsequent discussion, which focuses on the level surfaces of G and their interpretation as barriers. However, it is important to note that the functions $\tilde{\delta I}_1(\tau)$, $\tilde{\phi}_1(\tau)$, and $\tilde{\theta}_1(\tau)$ are required to address the stability of the barriers and the presence of chaos, a point that will be revisited in the concluding remarks.

D. Remarks on the number of possible resonant terms

It is obvious that if one resonant triplet $(n,m,\vec{l})$ satisfies the resonance condition (5) for a given torus I_0 and forcing frequencies $\vec{\sigma}$, then all harmonics of this triplet, namely, $k(n,m,\vec{l})$ where k is integer, are also resonant. So, in general, the sum in Eq. (14) contains an infinite number of resonant triplets. Note, however, that for the simplest case of a harmonic forcing with $\sin(\sigma t)$–time dependence [as in our numerical examples with the phenomenological model (1)], the only non-zero F^0_{nml} in the Fourier series (4) corresponds to $l=1$. Thus, even though summation in Eqs. (13) and (14) still includes all possible triplets $k\{n,m,l\}$, only the F^0_{nm1}-term under the sum has non-zero amplitude.

Another question one could ask is: "How many "non-harmonic" resonant terms can exist for a given torus?" The answer is different for resonant tori with periodic or non-periodic trajectories. When resonances occur with periodic trajectories of the background flow, the number of non-harmonic resonant terms is unbounded, whereas for non-periodic trajectories, the maximum number of non-harmonic resonant terms is 2.

To show this, we consider a non-periodic resonant trajectory of the background flow (with $\Omega_\phi/\Omega_\theta \neq M/N$ for any integers M and N), assume that it has three resonant triplets, and write down the resonance condition for the first two resonant triplets $\{n_{1,2}, m_{1,2}, \vec{l}_{1,2}\}$ and for the third triplet

$$\begin{aligned} n_1\Omega_\phi + m_1\Omega_\theta - \vec{l}_1\cdot\vec{\sigma} &= 0, \\ n_2\Omega_\phi + m_2\Omega_\theta - \vec{l}_2\cdot\vec{\sigma} &= 0, \\ n_j\Omega_\phi + m_j\Omega_\theta - \vec{l}_j\cdot\vec{\sigma} &= 0. \end{aligned} \quad (16)$$

We remind the reader that all forcing frequency components σ_i can be assumed to be incommensurate, otherwise a reduction of the number of frequency components would be possible (for example, a function with $\sigma_1 = 2\pi/2$ and $\sigma_2 = 2\pi/3$ is simply periodic with frequency $2\pi/6$). To simplify the analysis, it is convenient at this point to introduce a new set of frequencies $\hat{\sigma}_i = \vec{l}_i\cdot\vec{\sigma}$, so the above system becomes

$$n_i\Omega_\phi + m_i\Omega_\theta - \hat{\sigma}_i = 0, \quad i = 1,2,3. \quad (17)$$

Using the first two equations ($i=1$, 2) of system (17), we can express

$$\begin{aligned} \Omega_\theta &= \frac{n_1\hat{\sigma_2} - n_2\hat{\sigma_1}}{m_2n_1 - m_1n_2}, \\ \Omega_\phi &= \frac{m_2\hat{\sigma_1} - m_1\hat{\sigma_2}}{m_2n_1 - m_1n_2}. \end{aligned} \quad (18)$$

Note that since we are considering non-periodic trajectories, all forcing frequencies $\hat{\sigma}_i$, $i=1$, 2, 3 need to be incommensurate, otherwise it follows from the above equations (18) that the ratio $\Omega_\phi/\Omega_\theta = M/N$ with integers M and N, so the trajectory is periodic. With (18), the third equation in (17) becomes

$$(m_2n_3 - m_3n_2)\hat{\sigma_1} + (m_3n_1 - m_1n_3)\hat{\sigma_2} + (m_1n_2 - m_2n_1)\hat{\sigma_3} = 0. \quad (19)$$

Since n_i, m_i, and l_i ($i=1$, 2, 3) are integers, and all forcing frequencies $\hat{\sigma}_i$ ($i=1$, 2, 3) are incommensurate, the above equation can only be satisfied if the coefficients in front of each $\hat{\sigma}_i$ are zero, requiring that

$$(m_1n_2 - m_2n_1) = 0. \quad (20)$$

However, if $(m_1n_2 - n_2m_1) = 0$, then from (17) it follows that $\hat{\sigma}^1$ and $\hat{\sigma}^2$ are commensurable, $\Omega_\phi/\Omega_\theta = M/N$, and the trajectory in question is periodic, which violates our basic assumption. Hence, no more than 2 non-harmonic resonant terms can exist for any non-periodic trajectories.

Thus, when resonances occur with non-periodic trajectories of the background flow, the right-hand sides of Eqs. (13) and (14) can have at most two non-harmonic triplets, with at most two corresponding η_{nml}'s that are not integer multiples of each other. For periodic trajectories, on the other hand, the existence of one resonant triplet $(n,m,\vec{l})$ implies the existence of infinitely many non-harmonic triplets plus all their higher-order harmonics.

In the following, we will refer to the case with 1 non-harmonic resonant triplet as the single-resonance, and to the case with ≥ 2 non-harmonic triplets as the double-resonance. Using this terminology, resonances occurring with the periodic trajectories of the background flow are always of

the double-type. Resonances occurring with the non-periodic trajectories of the background flow are always of the single-type when the perturbation is periodic (only one forcing frequency σ_i in Eq. (4)), but could be either single- or double-type when the perturbation is quasi-periodic (≥ 2 σ_i's in Eq. (4)).

These observations also follow naturally from the intuitive plane wave description introduced in Subsection III A, where resonances result from the phase locking between the plane wave representing the disturbance and the motion of the fluid parcel. For a double-resonance, the trajectory is simultaneously phase locked with at least two plane waves (m_1, n_1, l_1) and (m_2, n_2, l_2), whose phase lines are aligned in different directions (Figure 2(b)). The particle must move so as to maintain constant phase with respect to both disturbances, so the intersection point between the two phase lines must coincide with the parcel trajectory. If the disturbance is periodic, the intersection point must eventually return to its initial location. The trajectory, which follows the intersection, must also return to its initial location and must therefore be periodic. Thus, only tori with periodic trajectories are subject to double resonance with respect to a single forcing frequency. On the other hand, when the forcing is quasiperiodic, and due to two incommensurate frequenciesis, the intersection point does not recur periodically and the corresponding resonant particle trajectory is aperiodic. Thus, quasiperiodic time dependence allows tori with non-periodic orbits to become double-resonant.

Finally, it is useful to think about the linear independence of the $\eta_{nml\vec{l}}$'s in (14). Suppose that we find one resonant triplet $(n_1, m_1, \vec{l}_1)$. We know that all of its harmonics, $2(n_1, m_1, \vec{l}_1)$, $3(n_1, m_1, \vec{l}_1)$ etc., are also resonant, but the corresponding arguments, $\tilde{\eta}_{2n_1,2m_1,2\vec{l}_1}$, $\tilde{\eta}_{3n_1,3m_1,3\vec{l}_1}$, etc., can be expressed as an integer multiples of $\tilde{\eta}_{n_1m_1\vec{l}_1}$ plus a constant. Using the plane-wave description, all of these disturbances propagate in the same direction and with the same normal phase speed. If there are no other resonant disturbances (as for the single-resonance case), then the solutions of (12) and (13) live in the two-dimensional space of $\tilde{\eta}_{n_1m_1\vec{l}_1}$ and $\tilde{\delta}I_0$. On the other hand, if the resonance is of the double type, then there is a second resonance disturbance $\tilde{\eta}_{n_2m_2\vec{l}_2}$ that is not a harmonic of the first disturbance. All of its harmonics are also resonant, but again, each can be written in terms of $\tilde{\eta}_{n_2m_2\vec{l}_2}$. In this case, solutions of (12) and (13) live in the three-dimensional space of $\tilde{\eta}_{n_1m_1\vec{l}_1}$, $\tilde{\eta}_{n_2m_2\vec{l}_2}$, and $\tilde{\delta}I$. Now suppose that we find a third resonant disturbance $\tilde{\eta}_{n_3m_3\vec{l}_3}$ that is not a harmonic of $\tilde{\eta}_{n_1m_1\vec{l}_1}$ and $\tilde{\eta}_{n_2m_2\vec{l}_2}$ (i.e., we have a double-resonance with a periodic trajectory). In this case, we have already shown in Subsection III C that the third disturbance can be expressed through a linear combination of the first two plus a constant, $\tilde{\eta}_{n_3m_3\vec{l}_3} = A\tilde{\eta}_{n_1m_1\vec{l}_1} + B\tilde{\eta}_{n_2m_2\vec{l}_2} + C$ with constant A, B, and C, so the phase space of (12) and (13) is still three-dimensional, even when there are three or more non-harmonic resonant triplets. This is intuitively clear as all phases $\tilde{\eta}_{nml\vec{l}}$ are functions of $\tilde{\phi}_0$ and $\tilde{\theta}_0$ following a resonant trajectory, and so at most two of them could be linearly independent. Graphically, $\tilde{\eta}_{n_3m_3\vec{l}_3}$ represents a plane wave that is not aligned with the other two. The resonance occurs when a fluid parcel follows a triple intersection point of the three phase lines with different orientations, corresponding to three disturbances. Here, it may be helpful to visualize the situation in a translating frame of reference in which the fluid parcel is stationary, so that the intersection point also becomes stationary. The plane-wave forms of the disturbances imply that their phase lines maintain fixed angles with respect to each other, and cannot rotate, so they must also appear as fixed lines in the translating frame. Then clearly, the vector $c_{n_3m_3\vec{l}_3}$ corresponding to the third wave can always be uniquely expressed in terms of its projections onto the first two vectors, $c_{n_1m_1\vec{l}_1}$ and $c_{n_2m_2\vec{l}_2}$. Thus, the third wave at any location is completely specified by the first two waves at that location.

Multi-scale analysis of resonances presented in Subsection III C of this paper apply to both periodic and quasi-periodic forcing (i.e., 1 or more forcing frequencies σ_i), both single- and double-resonances (i.e., 1 or more non-harmionic resonant triplets), and both non-degenerate and degenerate resonances (degenerate cases are described in the Appendix). Our results for the periodic forcing agree with Dullin and Meiss (2012), but the cases with quasi-periodic forcing and the case of a degenerate double-resonance are not considered in that paper.

IV. GEOMETRY OF THE FLOW NEAR RESONANCES AND RESONANCE WIDTH

We now focus on geometry of the invariant structures that arise within the resonant layer. In Sec. III, we found an integral of motion [see (14)] for the case, in which the first derivative of $n\Omega_\phi(I) + m\Omega_\theta(I)$ with respect to action at the resonant torus $I = I_0$ is nonzero. Cases of degeneracy, for which the first $j-1$ derivatives are zero, are treated in the Appendix, and result in a generalized integral in motion [see (A10)]. We now consider this generalized function G in the un-scaled variables δI (which to leading order is $\epsilon^{\frac{1}{j+1}}\tilde{\delta I}$) and $\eta_{nml\vec{l}}$ (which to the leading order is $\tilde{\eta}_{nml\vec{l}}$)

$$G = \frac{\delta I^{j+1}}{(j+1)!} + \epsilon \sum_{n,m,\vec{l}}^{resonant} \frac{F^0_{nml}(I_0)\cos(\eta_{nml\vec{l}})}{\frac{d^j(n\Omega_\phi + m\Omega_\theta)}{dI_j}\Big|_{I_0}}. \tag{21}$$

To a first approximation, fluid trajectories in the vicinity of a resonant torus are confined to the level surfaces of G. In the primitive time coordinate, with τ replaced by $\epsilon^{\frac{j}{j+1}}t$, the trajectories are given by $\phi(t) = \Omega_\phi(I_0)t + \tilde{\phi}_0(\epsilon^{\frac{j}{j+1}}t)$, $\theta(t) = \Omega_\theta(I_0)t + \tilde{\theta}_0(\epsilon^{\frac{j}{j+1}}t)$, and

$$\dot{\delta I} = \epsilon \sum_{nml\vec{l}}^{resonant} F^0_{nml\vec{l}}(I_0)\sin(\eta_{nml\vec{l}}), \tag{22a}$$

$$\dot{\eta}_{nml\vec{l}} = \frac{d^j(n\Omega_\phi + m\Omega_\theta)}{dI_j}\Big|_{I_0}\frac{(\delta I)^j}{j!}, \tag{22b}$$

with $\eta_{nml\vec{l}} = n\tilde{\phi}_0(\epsilon^{\frac{j}{j+1}}t) + m\tilde{\theta}_0(\epsilon^{\frac{j}{j+1}}t) + \alpha_{nml\vec{l}}$.

Evaluating G for a given flow is numerically challenging because it requires finding explicit expressions for the action-angle-angle variables (I, θ, ϕ) in terms of (x, y, z), finding the resonant torus I_0 along with the resonant sets $(n, m, \vec{l})$, Fourier expanding the perturbation to compute

$F^0_{nml}(I_0)$'s, and estimating the derivative terms in the denominator of (21). However, the qualitative geometry of the G-contours is not sensitive to the exact values of the coefficients, but is different for even and odd j and depends on the number of resonant terms η_{nml} in the right hand side of (21). For a resonance with 2 η's, the cases with both even and odd j are illustrated in Fig. 3 using $\frac{d^j(n_1\Omega_\phi+m_1\Omega_\theta)}{dI^j} = \frac{d^j(n_2\Omega_\phi+m_2\Omega_\theta)}{dI^j} = 1$, $\epsilon = 0.1$, $F_{n_1m_1l_1} = F_{n_2m_2l_2} = 1$, and all other F's $= 0$.

For both even and odd j, far from the resonant torus (i.e., large δI), G-contours flatten out and approach $\delta I \approx const$ (black surfaces in Fig. 3), suggesting that the corresponding unperturbed tori are only slightly distorted by the forcing. On the other hand, for small δI, trajectories are strongly affected by the resonance and undergo a major distortion (green and red surfaces in Fig. 3). Thus, the phase portrait of G can be split in two distinct regions—trajectories trapped inside the resonance, where $\delta I(t)$ crosses zero following a trajectory due to the sin -terms in the right-hand-side of Eq. (22a), and trajectories exterior to the resonance for which $\delta I(t)$ does not cross zero. This is equivalent to defining the resonance as the region where at least one η-variable wraps around following a trajectory, whereas outside of the resonance, all η's increase monotonically. In principle, the resonant region could be further divided into subdomains where either all η's wrap around or some η's wrap around and some increase monotonically, but here we are interested in defining the outer boundary of the resonant region rather than its sub-boundaries.

The interior and exterior of the resonant region are separated by a contour G_{sep}—the last G-contour that crosses $\delta I = 0$ (blue surface in Fig. 3). The upper bound on G_{sep} can be found by setting all cosines equal to 1 in (21):

$$G_{sep} = \epsilon \sum_{n,m,\vec{l}}^{resonant} \frac{|F^0_{nml}(I_0)|}{\left|\frac{d^j(n\Omega_\phi+m\Omega_\theta)}{dI_j}\right|_{I_0}}. \tag{23}$$

Note that this upper bound might not be reached for resonances that involve at least one linearly-dependent η-term. The maximum excursion in δI of this G_{sep}-contour can be used to define the upper bound on the width of the resonant region

$$\Delta I = 2\left(\epsilon(j+1)! \sum_{n,m,\vec{l}}^{resonant} \frac{|F^0_{nml}(I_0)|}{\left|\frac{d^j(n\Omega_\phi+m\Omega_\theta)}{dI_j}\right|_{I_0}}\right)^{1/(j+1)}. \tag{24}$$

The resonance width expression (24) is a generalization of formula (3.13) from Pratt *et al.* (2014) and reduces to their (3.13) for a single-resonance case with a steady disturbance. Again, the computation of a resonance width for a particular flow is numerically challenging because it requires Fourier-expanding the perturbation in terms of action-angle-angle variables. However, trends such as the ϵ-dependence and the dependence on the derivative term in the denominator of (24) have been tested against numerical simulations in a steady rotating can flow in Pratt *et al.* (2014), and good agreement was found. Note also that the n and m in denominator of (24) tend to create larger widths for low-order resonances (with small n and m). If the forcing produces a disturbance with broad spatial scales, then F^0_{nml} are also largest for small n and m, and a combination of large numerator and small denominator results in wide resonant layers for low-order resonances. On the other hand, if the forcing has fine spatial structure, then F^0_{nml} may be small for small n and m, and the situation is less clear.

In the simplest special case of a single-resonance excited by a harmonic forcing (i.e., the case with exactly 1 resonant triplet nml), system (22) becomes Hamiltonian

$$\begin{aligned} \dot{\delta I} &= -\partial G/\partial\eta, \\ \dot{\eta} &= \partial G/\partial(\delta I), \end{aligned} \tag{25}$$

with

$$G = \epsilon F^0_{nml}(I_0)\cos(\eta) + \frac{(\delta I)^{j+1}}{(j+1)!}\frac{d^j(n\Omega_\phi+m\Omega_\theta)}{dI_j}\Big|_{I_0} \tag{26}$$

playing the role of the Hamiltonian. The corresponding phase space geometry of system (26) is shown in Fig. 4 for odd and even j (again, using $\epsilon = 0.1$, $F^0_{nml}(I_0) = 1$ and $\frac{d^j(n\Omega_\phi+m\Omega_\theta)}{dI_j}|_{I_0} = 1$). For the simplest case of a non-degenerate single-resonance with j = 1, we recover the

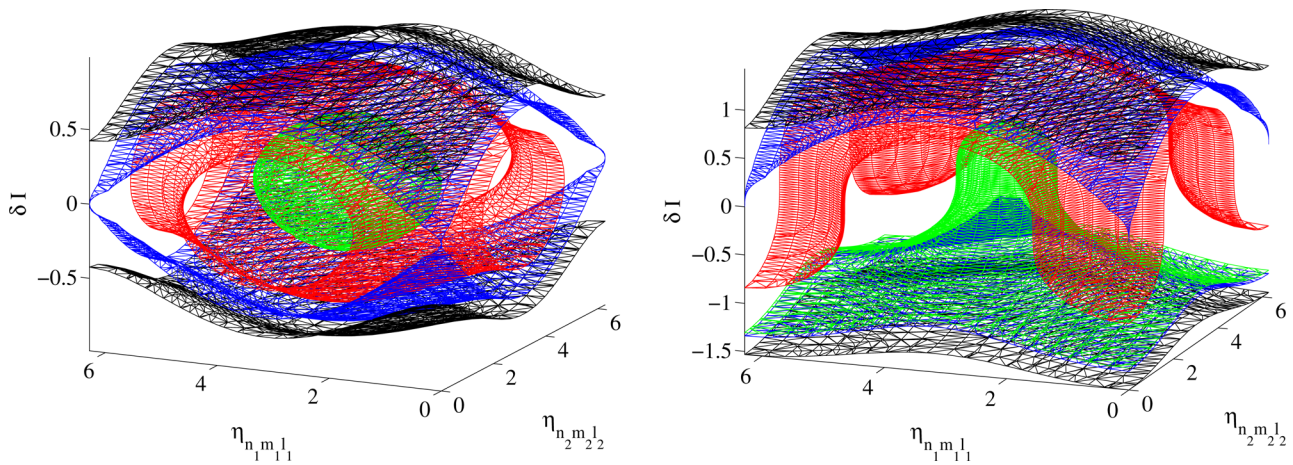

FIG. 3. In the case of a double-resonance, phase portrait of G for (left) odd and (right) even j.

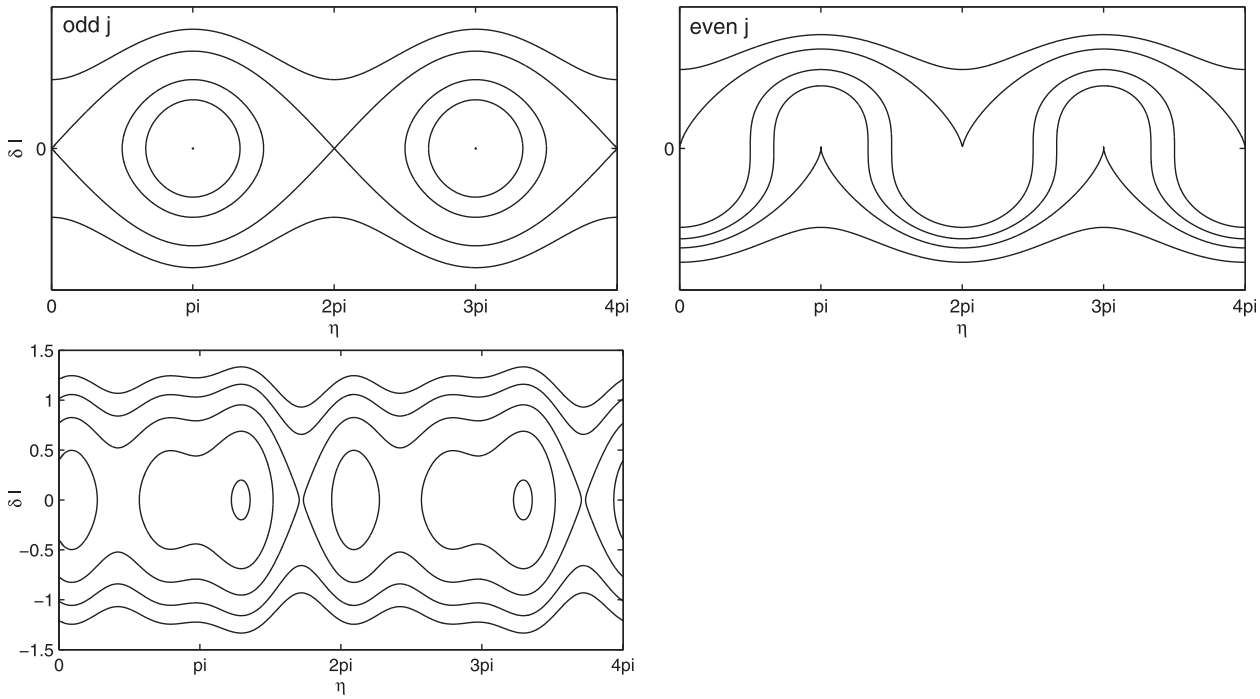

FIG. 4. Phase portrait of H for (top left) odd and (top right) even j. Phase portrait of G for $j=1$ with 3 harmonic sin-terms.

pendulum approximation geometry commonly observed in perturbed Hamiltonian systems.

The inclusion of harmonic and linearly-dependent terms in Eq. (21) leads to "modulation" of the G-surfaces, and an example with three harmonic terms, $\eta_{n_1m_1l_1}$, $\eta_{n_2m_2l_2} = 2\eta_{n_1m_1l_1} + \alpha_2$, and $\eta_{n_3m_3l_3} = 3\eta_{n_1m_1l_1} + \alpha_3$, is shown in Fig. 4 (bottom) for $j=1$, $\alpha_2 = 2.1$, $\alpha_3 = 2.7$, $\epsilon = 0.1$, $F^0_{n_im_il_i}(I_0) = 1$, and $\frac{d\left(n_i\Omega_\phi + m_i\Omega_\theta\right)}{dI}|_{I_0} = 1$ for $i=1, 2, 3$. The phase space can still be split into the resonant region where G-contours cross $\delta I = 0$ and the region outside of the resonance where G-contours do not cross zero. However, within the resonant region, additional elliptic and hyperbolic points arise leading to a more complicated geometry than for a simple pendulum approximation. As discussed above, the contribution of the higher-order terms tends to decrease with increasing order for disturbances with broad spatia l scales, so the modulation of the G-surfaces by higher-order harmonic terms is expected to be less pronounced than in Fig. 4 (bottom).

A. Geometry of the flow near resonances in the real physical space (*x, y, z*)

The level surfaces of G are material surfaces that sweep around the undisturbed resonant torus. Physical visualization of these surfaces, and the trajectories that follow them, is challenging due to the practical difficulty of computing the transformations from $(\delta I, \eta_{n_1m_1\vec{l}_1}, \eta_{n_2m_2\vec{l}_2})$ to $(\delta I, \phi, \theta)$ to (x, y, z). For most realistic flow fields, the second transformation is fiendishly difficult. However, since we are only interested in a qualitative geometry of the flow near resonances, progress can be made by assuming that all unperturbed tori are horizontal with circular cross-sections, and that ϕ and θ are the simple toroidal angles related to x, y, z by

$$\begin{aligned} x &= (R + r\cos\phi)\cos\theta, \\ y &= (R + r\cos\phi)\sin\theta, \\ z &= r\sin\phi, \end{aligned} \tag{27}$$

where $r = r_0 + \delta r = \sqrt{r_o^2 + \delta I/\pi}$ is the difference in radius from the reference torus, r_0 is the radius of the vertical cross-section of the reference torus, and R is the distance from the center of the reference torus to the vertical axis of symmetry. The last expression follows from the fact that we define action I as an area of a vertical cross-section of a torus, so δI is the difference in area from the reference torus.

The geometry of the flow near different single-resonances in $(\eta_{n_1m_1l_1}, \eta_{n_2m_2l_2}, \delta I)-$, $(\theta, \phi, \delta I)-$, and $(x, y, z)-$spaces is illustrated in Fig. 5 for $(n, m, l) = (0, 1, 1)$ (first row), (2, 0, 1) (second row), and (1, 1, 1) (third row). In all subplots, the outer blue G-surface represents a separatrix bounding the resonant region, with all outer surfaces (not shown) being topologically equivalent to the unperturbed tori. Inside the blue surface lie the red and green surfaces. The green surface lies close to the $\delta I = 0$ contour, which in (x, y, z) corresponds to an invariant closed curve located at the very center of the resonant region. The red surface lies between the green and the blue. The (0, 1, 1)-case that is shown in the upper panels corresponds to the 1:1-resonance between the forcing frequency and Ω_θ, so θ is a resonant coordinate and ϕ is a non-resonant coordinate. Thus, the red and green surfaces in the top right panel, as well as all other G-contours lying inside the blue separatrix, occupy a limited range in θ, but extend all the way in ϕ from 0 to 2π (see the red surface for illustration). We will refer to this geometry as the "folded torus" geometry as opposed to the usual "unbroken tori." If one plots G-surfaces lying just outside/inside of the red one, the gap between the two edges of the

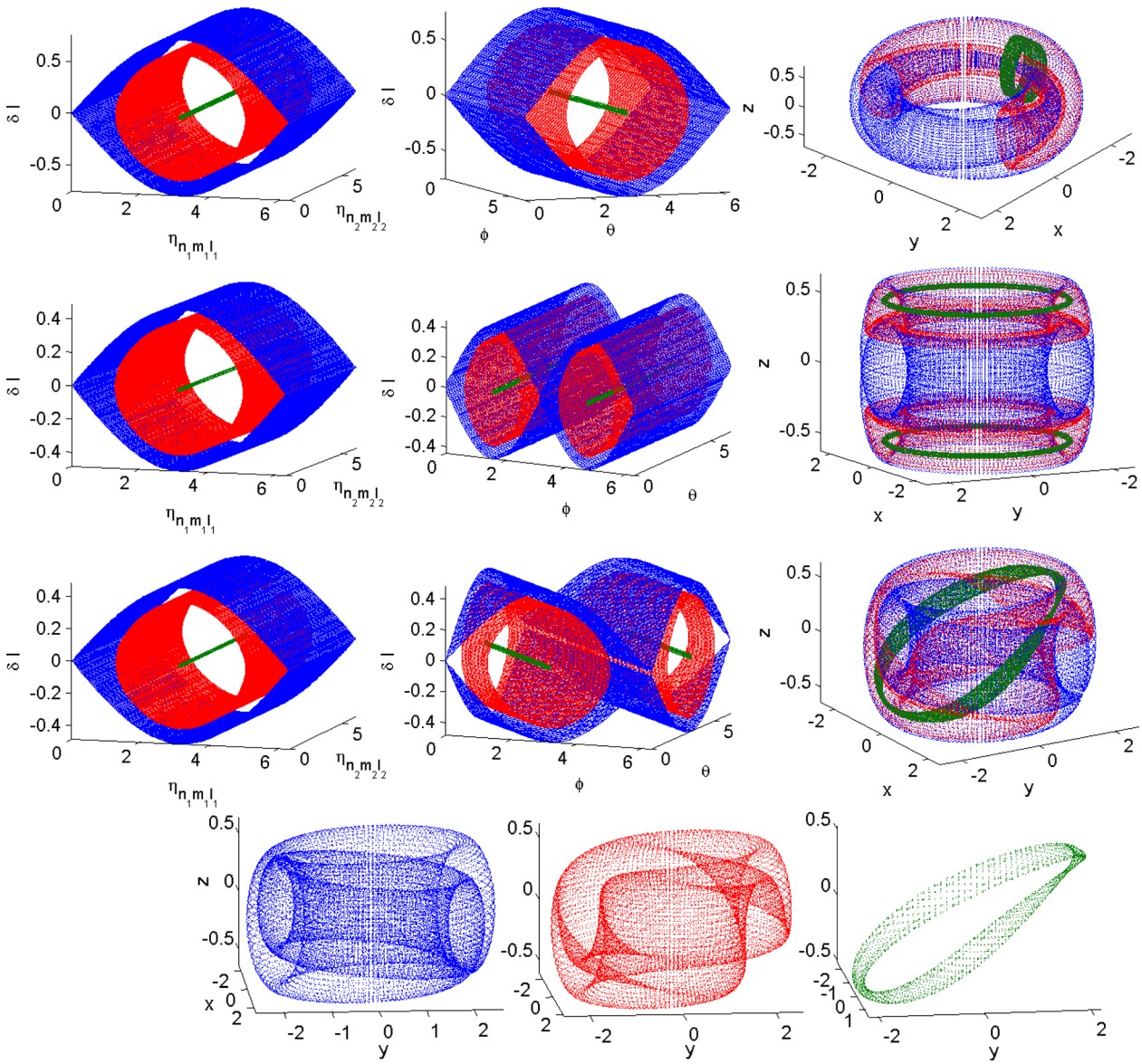

FIG. 5. Geometry of the G-surfaces in $(\eta_{nml}, \delta I)$-space (left), $(\theta, \phi, \delta I)$-space (middle), and in the real physical (x, y, z)-space (right) for three different single-resonances: (first row) $(n, m, l) = (0, 1, 1)$, (second row) (2, 0, 1), and (third row) {1, 1, 1}. The three small panels show the blue, red, and green objects from the right panel of the third row.

folded torus gets smaller/larger, respectively, shrinking to zero as we approach the separatrix (blue) or extending to 2π as we approach the closed invariant curve (green) at the center of the resonant region. Similarly, for the (2, 0, 1)-resonance in the second row panels, θ is a non-resonant and ϕ is a resonant coordinate, leading to all surfaces within the blue separatrix being discontinuous in ϕ with 2 gaps. Again, both the top and bottom halves of the red surface in the right middle panel have the altered "folded torus" geometry. As before, for larger and larger G-surfaces containing the red one, the gaps between the top and bottom parts get smaller until the top and bottom touch each other at the separating blue surface. For smaller and smaller surfaces contained within the red object, the gaps get larger until eventually we approach the green closed invariant curve. The (1, 1, 1)-resonance in the 3 bottom panels is not very different from the other two single-resonance cases. In the bottom right panel, we again have the folded torus geometry, but instead of having a vertical or horizontal gap in the folded torus as in the top and middle panels, respectively, the gap now wraps around the torus making one complete loop in both ϕ and in θ before connecting back to itself. More generally, the gap loops n times in ϕ and m times in θ before connecting to itself.

G-surfaces for a double-resonance with two non-harmonic resonant triplets, (1, 0, 1) and (0, 1, 1), are shown in Fig. 6. Two qualitative differences between this figure and the single-resonance in Fig. 5 are that: (1) some of the G-surfaces have a torus-knot or pretzel-like geometry, and (2) the surfaces are centered around fixed points in η-δI-space (representing isolated periodic orbits in (x, y, z)) rather than around closed invariant curves, so that G-surfaces lying near the center of the resonant region have spherical rather than toroidal geometry. In Cartesian (x, y, z)-coordinates (left middle panel), the blue separatrix consists of the inner and outer tori, where the inner torus just touches the outer

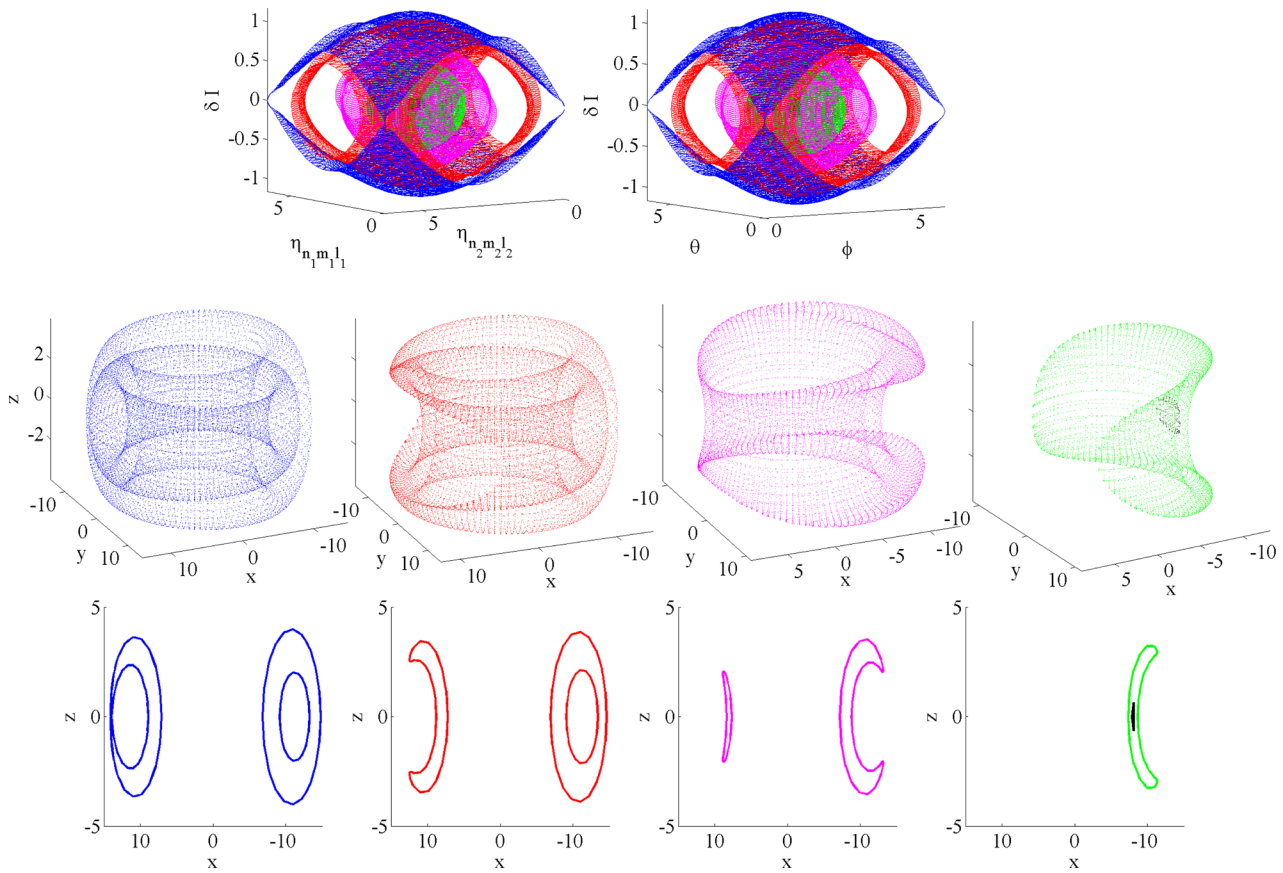

FIG. 6. Geometry of the G-surfaces for a double-resonance with two independent resonant triplets, (1, 0, 1) and (0, 1, 1), in $(\eta_{nml}, \delta I)$-space (top left), $(\theta, \phi, \delta I)$-space (top right), and in the Cartesianl (x, y, z)-coordinates (middle panels). A slice at $y = 0$ through each object is shown in the bottom panels.

one at one point at the very left of the left middle panel. This is further illustrated in the left bottom panel by taking a slice through the blue object at $y = 0$. The red surface lying just within the blue has openings both in θ and ϕ in the $(\theta, \phi, \delta I)$–space (upper right panel), and thus has a hole leading to the inside of the smaller torus in (x, y, z)-space. As we look at tori lying inside the red surface in the $(\theta, \phi, \delta I)$–space (upper right panel), both gaps in θ and ϕ shrink, until eventually the gap in θ disappears. All smaller surfaces will thus be qualitatively similar to the purple object, which have a gap in ϕ but not θ. In (x, y, z)-coordinates (right middle panel), the purple object is topologically equivalent to the folded tori we saw in the single-resonance cases. Finally, as we go to smaller and smaller surfaces contained within the purple, the gap in ϕ will eventually close up in the $(\theta, \phi, \delta I)$–space, and all smaller G-surfaces will have spheroidal geometry similar to the green and black objects.

B. Strong KAM stability

Resonance widths are important because overlapping resonances lead to the destruction of all tori between them, initiating the onset of widespread chaos (Chirikov, 1979; Zaslavsky and Chirikov, 1972). The resonance condition (5) is formulated in terms of frequencies, so the resonance overlap criterion is most easily defined in the frequency domain as $\Delta\Omega \geq \Omega_1 - \Omega_2$, where $\Omega_{1,2}$ are the neighboring resonant frequencies and $\Delta\Omega$ is the width of a resonance in frequency domain,

$$\Delta\Omega = \frac{\partial^j \Omega}{\partial I^j}(I_0)\frac{(\Delta I)^j}{j!} \propto \epsilon^{j/(j+1)}, \tag{28}$$

with ΔI given by (14). The scaling $\Delta\Omega \propto \epsilon^{j/(j+1)}$ suggests that resonance widths are generally smaller when j gets larger. Thus, degenerate resonances with $j > 1$ generally have smaller resonance widths than nondegenerate resonances with $j = 1$. So, degenerate resonances generally require larger perturbation strength to overlap, leading to the greater resistance to chaos near degenerate tori. This phenomenon is referred to as the "Strong KAM Stability" near degenerate tori. It is similar to the strong KAM stability in 2D flows (Rypina *et al.*, 2007b), which is responsible for the existence of robust transport barriers near shearless trajectories at jet cores in oceanic and atmospheric flows.

V. NUMERICAL EXAMPLES

In this section, we test the above results numerically by constructing examples of resonances for the "rotating can" flow described in Sec. II. We focus on most generic single-resonance cases; double-resonances are less typical and more challenging to produce numerically. We also restrict our attention to the simplest periodic perturbation because it allows us to use Poincaré section techniques to visualize the resonant objects. Quasi-periodic perturbation cases are not

well-suited to treatment by the Poincaré sections and require other methods of visualization. We will come back to this in Sec. VI.

Visualizing 3D time-varying objects, such as oscillating tori, could present a challenge. One way to overcome this challenge is by sampling the object at the same phase, so the oscillation is eliminated and the object appears steady. For time-periodic systems, this is achieved by temporal Poincaré strobing, where samples are taken at integer multiples of the forcing period T, i.e., at discrete times $t\sigma = 0 \mathrm{mod}(2\pi)$. Once a steady 3D object has been constructed via the above-described temporal Poincaré strobing, a vertical slice through the object at $\theta = \text{const}$ can be made to reduce it to two dimensions r and z (we use $|\theta| = \pi/2$ or, equivalently, $y = 0$). We will refer to the resulting 2D slice as the double Poincaré section. On the double Poincaré section, periodic trajectories will appear as stationary points, regular trajectories that live on oscillating tori will correspond to discretely sampled closed curves, whereas chaotic trajectories will appear as scattered dots that fill finite areas.

A. Resonances in the phenomenological model of the rotating can flow

In order to use the resonance condition (5) to define the forcing frequencies that will excite resonances in our phenomenological model of the rotating can flow, we have numerically estimated T_ϕ and T_θ for trajectories of the unperturbed axially symmetric background flow. As shown in Fig. 7 (top right), T_θ spans the range from about 9 to 10.7 and T_ϕ spans the range from about 8.7 to 15. A periodic trajectory with period $T_\phi = T_\theta \approx 10$ exists, which corresponds to a stationary point on the Poincaré section of the unperturbed flow (Fig. 7 (top left)) and which gives rise, when a steady symmetry-breaking disturbance is added (Eq. (1) with $\gamma = 0$), to one large island in Fig. 7 (bottom). At the center of the island lies a steady elliptic point (corresponding to a periodic trajectory in 3D), surrounded by a family of nested closed curves (twisted tori in 3D). Some of the original tori are deformed but remain unbroken, they are centered near $x = -0.33$ and $z = 0.4$ in the left-hand part of the section; we will refer to this region as a "central region." The region near the cylinder axis ($x = 0$) and around the perimeter of the can become chaotic and appears as a cloud of scattered dots in Fig. 7 (bottom). Because the system is steady in both Fig. 7 (top) and (bottom), no temporal Poincaré strobing is necessary and both Poincaré sections simply correspond to the vertical section at $\theta = 0$ through the cylinder.

We now test the system's response to harmonic time-periodic forcing for three different choices of the forcing period: $T_f = 1$, 4.5, and 11.05. The first choice is "very weakly resonant" in the sense that the corresponding forcing frequency $\sigma = 2\pi/T_f = 2\pi$ is far from both Ω_ϕ or Ω_θ for all trajectories in the background flow. Thus, according to (5), no low-order resonances can be excited by this forcing, and the corresponding double Poincaré section for the unsteady system in Fig. 8 (top) is topologically similar to the Poincaré section for the steady perturbed system (Fig. 7 (bottom)). Both sections show nested unbroken tori in the central region (one such torus is shown in Fig. 8 (top right) after temporal Poincaré sampling was done to eliminate its time-periodic oscillation), an island, and a chaotic zone near the perimeter of the cylinder.

The second forcing considered ($T_f = 4.5$) is resonant with one of the nested tori lying in the central region. In the background flow, this is the torus with trajectories whose T_ϕ is twice the forcing period, i.e., $\sigma/\Omega_\phi = 2$, so the corresponding resonant triplet in (5) is $n = 2$, $m = 0$, and $l = 1$. No other low-order resonances are excited by this forcing

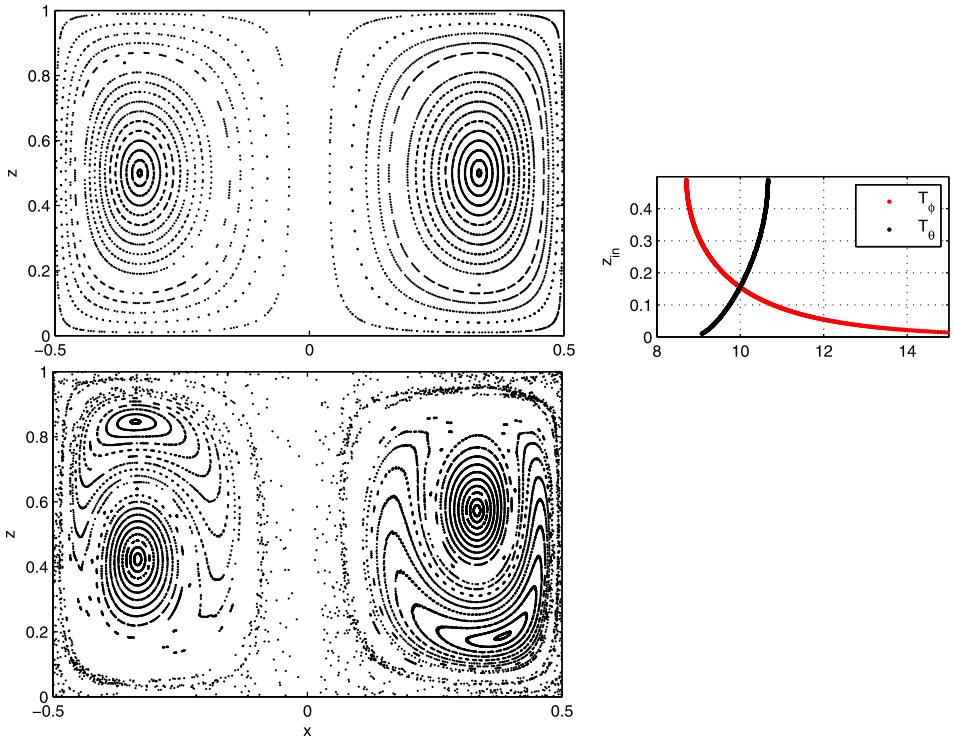

FIG. 7. (top left) Poincaré section for the unperturbed flow. (top right) Periods of trajectories in the unperturbed system. Trajectories were released at initial positions $x_{in} = 0.333$, $y_{in} = 0$, and different z_{in} spanning the range $0 < z_{in} < 0.6$. (bottom) Poincaré section for the steady perturbed system.

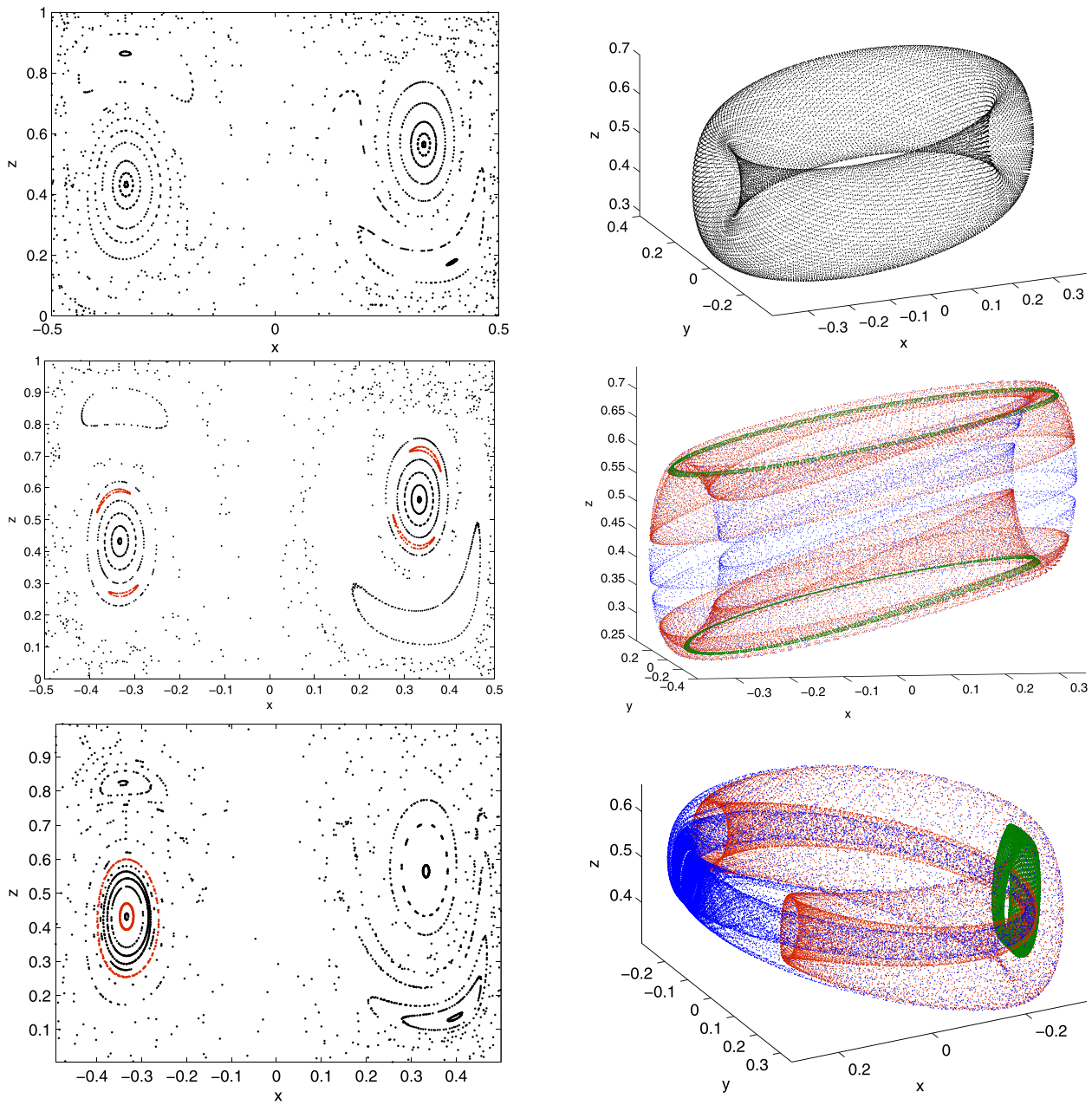

FIG. 8. For the periodically-perturbed phenomenological model of the rotating cylinder, the Double Poincaré section (left) and the corresponding 3D geometry (right) for the three choices of forcing frequency: (top) $T_f = 1$, (middle) $T_f = 4.5$, and (bottom) $T_f = 11.05$.

frequency. The corresponding double Poincaré section in Fig. 8 (middle left) looks topologically similar to the steady perturbed Poincaré section in Fig. 7 (bottom) everywhere except near the above-mentioned resonant torus. There is still a chaotic zone near the cylinder perimeter, and one large island produced from the break-down of the periodic trajectory. However, the central region around $x = -0.33$ and $z = 0.4$ in the left-hand part of the section, which only contained nested unbroken tori in Fig. 7 (bottom), now shows a new resonant structure (shown in red) that appears as two islands on the double Poincaré section in Fig. 8 (middle left). The corresponding 3D geometry (after temporal Poincaré sampling) of this resonant structure, shown in the right panel, is qualitatively similar to Fig. 5 (right panel of the 2nd row). Both the top and bottom halves of this object look like "folded tori," where the bottom (top) part of the torus was folded inside its top (bottom) part. The object is continuous in θ because this is a non-resonant coordinate (i.e., $m = 0$) but is discontinuous in ϕ with two islands in each vertical slice (because $n = 2$). The red torus is, of course, just one out of the whole family of tori whose geometries have been altered by the resonance. All of these tori are topologically similar and are contained one within the other. The blue torus, for example, lies just outside of the red, and its top and bottom halves come closer together. If we continue to plot other tori that contain the red and the blue tori, eventually for one of those, the top and bottom halves will extend all the way in ϕ and touch each other, forming a separatrix. Close to the separatrix, the flow is chaotic. Far from the resonance, outside of the separatrix, tori are only very weakly affected by the resonance and survive the perturbation. If we go in the other direction and plot smaller and smaller tori

that are contained within the red one, the top and bottom halves will get further and further from each other until eventually we hit the limiting trajectory that lives at the very core of the whole family of the top and bottom halves. This limiting trajectory corresponds to two closed curves on the 3D temporal Poincaré section in Fig. 8 (middle right) (i.e., after stroboscopic sampling at the forcing period). Each of these two closed curves intersects twice with the vertical $y=0$-plane (once at $x<0$ and once at $x>0$), giving a pair of period-2 elliptic points lying at the centers of the red islands in Fig. 8 (middle/left). The green object in Fig. 8 (middle right) is an example of a torus that lies very close to that limiting trajectory.

The third choice of the forcing, $T_f=11.05$, is also resonant and excites the lowest-order resonance with one of the nested tori in the central region. In the background flow, trajectories that foliate this torus have $T_\theta=T_f$ or, equivalently, $\sigma/\Omega_\theta=1$. The corresponding resonant triplet in Eq. (5) is therefore $n=0$, $m=1$, and $l=1$, and the corresponding resonant geometry is equivalent to Fig. 5 (right panel of the 1st row). As before, no other low-order resonances are excited by this forcing. Similar to the case with $T=4.5$, the double Poincaré section for $T=11.05$ in Fig. 8 (lower left) looks qualitatively similar to the steady perturbed Poincaré section in Fig. 7 (bottom) everywhere except near the resonant torus. There, a resonant structure is now present, which looks like two concentric red circles (both circles are produced by the double Poincaré strobing of the same trajectory) in the left part of the section ($x<0$) with no signature at $x>0$. As shown in the right bottom panel of Fig. 8, this resonant object is continuous in ϕ because this is a non-resonant coordinate (i.e., $n=0$) but discontinuous in θ with 1 gap (since $m=1$). This is topologically equivalent to Fig. 5 (right panel of the 1st row). Again, we can find the whole family of tori whose geometies are qualitatively similar to that of the red object. As we look for tori that contain the red object, eventually, we will hit the separatrix (blue object is very close to the separatrix) that extends all the way in θ and touches itself. Outside of this separatrix, tori are only weakly affected by the resonance, so they are slightly distorted but still maintain the usual unbroken torus geometry. As we look at tori such as the green one that are contained within the red, the objects shrink in θ-direction until eventually we hit the invariant closed curve at the very core of the nested family of objects.

Finally, it is important to note that the resonant flow geometries described above are quite robust with respect to the small changes in the forcing frequency. Because the periods of trajectories vary smoothly from one unperturbed torus of the background flow to the next, changing the forcing frequency will simply lead to a slight shift in the center position of the resonance towards the neighboring outer or inner torus but will not alter the qualitative geometry of that resonance.

B. Resonances in the full numerical solution for the rotating can flow

With the above geometries as a guidance, we now proceed to produce an example of a resonance using the full numerical solution of the Navier-Stokes equations. We used the Nek5000 model described in Sec. II, which was configured with 640 elements within the cylindrical domain with Legendre polynomials of order $N=11$, resulting in 1105920 mesh points. The dimensionless time step was 10^{-4}, and the tolerance for flow divergence was 10^{-9}. The time dependence became very nearly periodic after about 10 forcing periods, or about 4000 cpu hours, at which time the velocity fields over one forcing period were saved and used offline with bi-linear spatial and temporal interpolation for particle advection. As double stroboscopic sections require long trajectory integrations, the results are potentially sensitive to roundoff errors and to small violations of volume preservation (Speetjens and Clercx, 2005). The results for one case were compared with on-line trajectory calculation from a high resolution (N = 21, 6814720 mesh points) run to verify numerical convergence, and good agreement was found.

The steady axially-symmetric background and the corresponding periods of trajectories in the unperturbed system are shown in Fig. 9 (top). Here, T_θ varies from about 16 to 22, and T_ϕ from about 13 to over 100. Several low-order periodic trajectories are apparent in the top right panel of 9: A periodic trajectory with $T_\phi=T_\theta\approx 16.2$ is closest to the mid-depth of the can (near $z_{in}=0.39$), another periodic trajectory with $2T_\theta=T_\phi\approx 36$ exists (but is not shown in the top left panel) a little further from mid-depth near $z_{in}=0.13$, and other periodic trajectories with $T_\phi/T_\theta=M/N$ with large integer M and N lie closer to the perimeter of the cylinder. The middle panel of Fig. 8 shows the Poincaré section for the steady perturbation, where the lid of the cylinder has been shifted slightly off-center. Under the influence of this steady disturbance, each of the periodic trajectories breaks down producing chains of islands, with the largest and most prominent island corresponding to the break up of the periodic trajectory with $T_\phi=T_\theta\approx 16.2$. Qualitatively, this Poincaré section is similar to that for the phenomenological model, with the nested unbroken tori in the central region (which is now centered around $x=\pm 0.6$ and $z=0.65$), one large island outside of this region, and chaotic zone near the perimeter of the cylinder.

We now start to force the system by moving the lid periodically with period $T_f=16.35$ in x-direction around its shifted position. This forcing period is equal to T_θ for trajectories lying on a torus located roughly halfway between the periodic trajectory at $z=0.65$ and the perimeter of the can, just outside of the torus with periodic trajectories. The corresponding resonant triplet in Eq. (5) is $n=0$, $m=1$, and $l=1$, and the expected resonance geometry should be topologically equivalent to that shown in Figs. 5 (right panel of the 1st row) and 8 (bottom) (see also small inset in the right bottom panel of Fig. 9). Consistent with this expectation, on the corresponding double Poincaré section (Fig. 9 (bottom left)), the resonance (shown with large black dots) appears in the form of two concentric circles on the left half-plane ($x<0$) with no counterpart in the right half-plane. The black object is, of course, not the only one affected by the resonance. For example, a torus just next to it (shown using purple stars) has a similar geometry, but—unlike the black object—extends further in θ and appears as two concentric

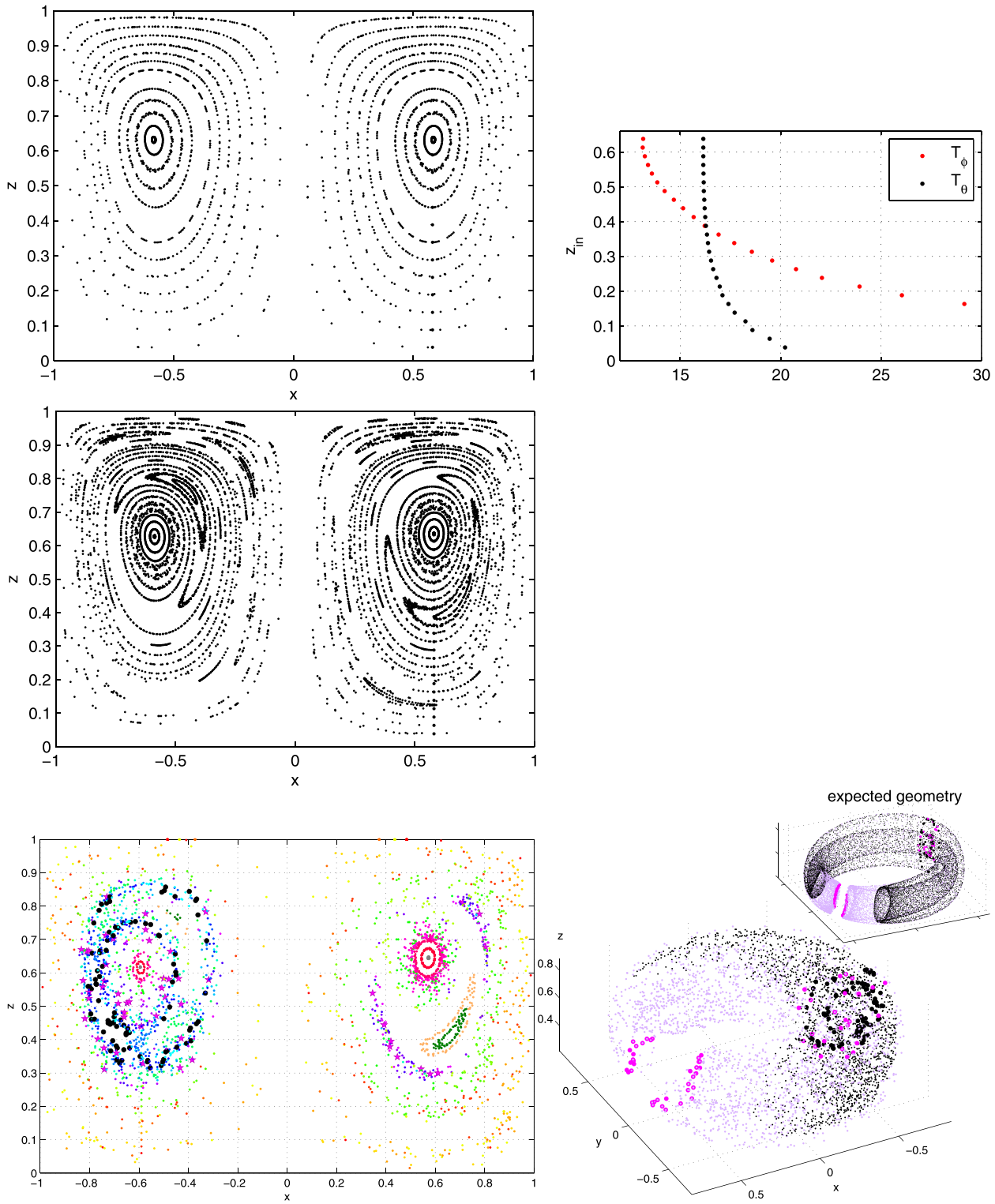

FIG. 9. For the full numerical solution of the flow in the rotating cylinder, the Poincaré section for the background axially-symmetric flow (top left), the corresponding trajectory periods (top right), the Poincaré section for the steady symmetry-breaking perturbation (middle), and the double Poincaré section for the time-periodic resonant disturbance of the upper lid (bottom). Small inset on the bottom right shows the expected resonance geometry in 3D inferred from the phenomenological model.

circles on one side of the double Poincaré section and as two separate islands on the other side. The 3D structure of both the black and purple objects is illustrated in the bottom right panel of Fig. 9. Both objects look noisier than their counterparts from the bottom right panel of Fig. 8 that were constructed using the analytically-prescribed phenomenological model. This is likely because the calculation of the double Poincaré section and the corresponding 3D geometries of the resonant objects require long trajectory integration of about $2000T_f$, which presents significant numerical challenges and unavoidably leads to some numerical noise due to interpolation errors. Spectral-solver (Speetjens and Clercx, 2005) or

volume-preserving integration schemes might help mitigating this problem and reduce numerical noise. Apart from this noise, however, the black and purple objects in Fig. 9 (bottom left) are topologically equivalent to the expected resonance geometry predicted by the theoretical arguments and numerical simulations in the phenomenological model. Note that we only expect topological similarity between the objects in Figs. 8 and 9 since they correspond to the same resonance type, but not exact equality between them because they belong to different flows. Note also that the velocities in the Navier-Stokes simulations, though time periodic, might not be exactly sinusoidal in time, as they were in the phenomenological model. Thus, harmonic terms with finer temporal scales may be present at low amplitude, thereby rendering invariant surfaces more difficult to resolve. It is possible that this has contributed to the less distinct character of the surfaces computed.

C. Resonances and tracers

From the physical oceanographic point of view, the double Poincaré sections are of limited use in the field or in the lab because real oceanic flows rarely remain intact over long time scales required to construct them. A more relevant question would be whether resonances have strong effect on the redistribution of tracers and other measurable physical quantities over time scales of several tens (rather than thousands) of forcing periods. To investigate this question, we numerically simulated, using the NEK5000 model, a release of a small compact blob of tracer in the rotating can flow with the resonant ($T_f = 16.35$) and non-resonant ($T_f = 14.5$) forcing, and looked at its subsequent evolution over 22 forcing periods. Initially, the tracer was confined to a small ellipsoid lying entirely in the interior of the black folded torus (one of those whose geometry was altered by the resonant forcing) shown in the bottom panels of Fig. 8. For a flow with the resonant forcing, and in the absence of any diffusion, this structure would represent a perfect impenetrable material barrier. When a small amount of diffusion is present, as in our numerical tracer release experiment (Peclet number $Pe = 10^5$ or, equivalently, dimensionless diffusivity $\kappa = 10^{-5}$), the tracer will slowly "diffuse" across that surface. However, because the diffusion process is slow, over relatively short time scales of several tens of forcing periods, the tracer has to remain mainly on the interior side of this boundary. Since the forcing is periodic, the boundary oscillates in time and is repeated after each forcing period. Hence, by taking snapshots of the tracer field at multiple integers of the forcing period, i.e., at $t = T_f, 2T_f, \ldots, 22T_f$, and then averaging together these snapshots, we can approximately reconstruct the geometry of the boundary (see also Mezic and Sotiropoulos (2002) for a rigorous discussion of this method).

The most striking geometric feature of the black folded torus is that, unlike unbroken tori of the background flow, it does not extend all the way around the can in θ and consequently does not intersect the vertical x-z plane at $x > 0$ (see left bottom panel of Fig. 8). The tracer, which is mostly confined within the black folded torus for the flow with resonant forcing and small diffusivity, also should have no (or very little) signature on the right side (i.e., at $x > 0$) of the x-z plane. Consistent with this picture, for the resonant forcing case shown in the left panel of Fig. 10, the bulk of the tracer concentration is observed on the left side of the x-z plane at $x < 0$, with much smaller tracer concentrations on the right side at $x > 0$. The little amount of tracer seen at $x > 0$ has leaked there by the slow diffusion process. To produce Fig. 10, we have renormalized each of the 22 tracer concentration snapshots to have values between 0 and 1 before averaging together all snapshots. Without such renormalization, snapshots taken at earlier times (i.e., when tracer has not dispersed much yet) have much higher tracer concentrations and thus dominate the averaged field. Renormalization evens out the contributions from different snapshots leading to a more representative picture of the areas occupied by and devoid of the tracer. Note that the renormalization does not in any way facilitate the "leakage" of the dye from the inside to the outside of the barrier, and thus does not corrupt the invariant structures.

In contrast to the resonant forcing case in Fig. 10(a), for the non-resonant forcing case shown in Fig. 10(b), the resonant island is completely absent and the tracer is not constrained to stay within the black folded torus. Instead, the tracer is free to spread azimuthally around the can all the way in θ, intersecting the vertical x-z plain both at $x < 0$ and $x > 0$. Thus, the corresponding averaged tracer concentration field in Fig. 10(b) shows comparable values on the left and right sides of the x-z plane.

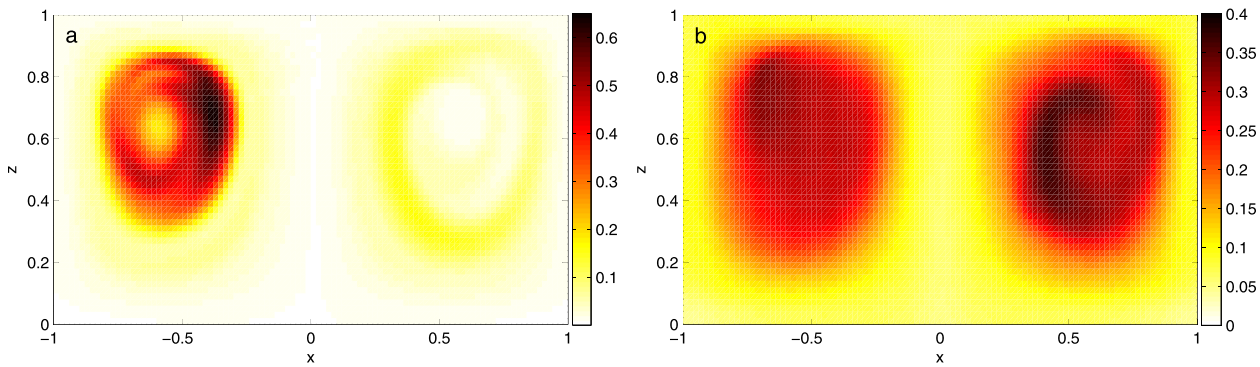

FIG. 10. Renormalized averaged tracer concentration in the x-z plane for the rotating cylinder flow with (a) resonant ($T_f = 16.35$) and (b) nonresonant ($T_f = 14.5$) forcing.

The numerical simulation just described illustrates the importance of resonances and suggests that small $O(10\%)$ change in the forcing period can lead to major qualitative changes in the resulting tracer distribution. Due to its simplicity, tracer experiments of this type can potentially provide a technique for studying resonance phenomena in the lab and in the field.

VI. DISCUSSION AND CONCLUSIONS

In this paper, we used a combination of weakly-nonlinear analysis and numerical simulations to clarify some important aspects of resonant chaotic stirring in certain classes of 3D time-dependent fluid flows with symmetries. Our analysis lead naturally to the resonance condition (5) predicting that resonances occur when the forcing frequency is commensurable with the frequencies of trajectories in the unperturbed flow. The flow in the vicinity of such resonant trajectories can be studied using multi-scale analysis leading to a simplified system (22). An important property of (22) is that it has an integral of motion G given by (21), so the behavior of trajectories can be understood by mapping out contour levels of G. Based on the relationship between the forcing frequency and frequencies of trajectories, resonances have been classified into single-resonances and double-resonances. Resonant geometries have been mapped out for a variety of single- and double-resonances, and general trends have been identified and discussed. The theoretically predicted geometries were compared to numerical simulations in both phenomenological model and in a full numerical solution of the Navier-Stokes equations for a rotating can flow, and a good agreement was found. Also, the expression describing the width of the resonant region—an important parameter for the set-up of global chaos—has been derived, and the physical interpretation of the resonances in terms of plain waves has been discussed.

Because frequencies of trajectories in the unperturbed system generally span a range of values, many resonances are excited by a given forcing frequency. Unless the forcing varies on a very fine spatial scale, the lowest-order resonances are generally the strongest. Higher-order resonances are usually confined to more narrow areas, and their impact on the overall flow geometry and properties is much weaker. When the forcing is time-harmonic with simple $\sin \sigma t$–time dependence, such as in our numerical examples, only resonant triplets with $l = 1$ are allowed in the resonance condition (5). However, for a more general time-dependence, each resonant triplet $\{n, m, l\}$ also has higher-order harmonics, $k * \{n, m, l\}$, which are usually less important than the main harmonic but whose influence cannot be completely ignored.

Single-resonances are very common because even the simplest time-harmonic single-frequency forcing is expected to excite multiple single-resonances with various trajectories. Double-resonances, on the other hand, are less typical and, for a time-periodic forcing, can only occur with periodic trajectories of the background flow. Quasi-periodic forcing can excite double-resonances with non-periodic trajectories, but only for very carefully chosen forcing frequencies (for example, when σ_1 is commensurable with Ω_ϕ and σ_2 with Ω_θ for the same trajectory).

It is natural to ask why the multiple scale expansion does not capture any of the chaotic behavior that arises in the model examples around and within resonant layers. Note that since the lowest order terms in (15) exhibit regular behavior, chaos would have to arise in the undetermined higher order corrections $\tilde{\phi}_1(\tau)$, $\tilde{\theta}_1(\tau)$ and $\delta\tilde{I}_1(\tau)$. However, since $\delta\tilde{I}_1(\tau)$, ϕ, and θ for a chaotic trajectory will depart by a large amount from their lowest order values δI_0, ϕ_0, and θ_0 for the G-conserving approximation, $\delta\tilde{I}_1(\tau)$, $\tilde{\phi}_1(\tau)$, $\tilde{\theta}_1(\tau)$ would eventually grow to $O(\epsilon^{-1/(j+1)})$, and the asymptotic approximation would be invalidated. One could certainly test for unbounded growth by computing $\delta\tilde{I}_1(\tau)$, $\tilde{\phi}_1(\tau)$, $\tilde{\theta}_1(\tau)$ through a consideration of higher order balances, which is not carried out here. This analysis, which addresses the stability of the G-conserving orbits, would at least identify the stable ones.

The restriction to time periodic flow is, of course, an idealization for ocean applications. Quasiperiodic and aperiodic time dependence raises significant conceptual, computational, and even visual challenges. Recent advances that attempt to confront these difficulties are based on measures of coherence, ergodicity, complexity, hyperbolicity, and other properties that potentially distinguish an "invariant" surface or barrier in a 3D flow with general time dependence. Specific approaches include variational methods for Lagrangian coherent structures (Beron-Vera *et al.*, 2013), transfer operators (Froyland *et al.*, 2007), ergodic quotient partitions (Budisic and Mezic, 2012), trajectory complexity measures (Rypina *et al.*, 2011), and Lagrangian descriptors (Mendoza *et al.*, 2014). It is not known how accurately or efficiently any of these methods would be able to reproduce the objects shown, say, in Fig. 8. Nor is it known whether any of the methods could capture the objects approximated in Fig. 9 with more clarity or economy. There are some promising results, for example, Budisic and Mezic (2012) are able to compute invariant surfaces and chaotic seas for the ABC flow, for which the velocity field is three-dimensional but steady, and for the periodically-forced three-dimensional Hill's vortex flow. Blazevski and Haller (personal communication) were able to compute one of the time-periodic invariant surfaces from our kinematic model using the Beron-Vera *et al.* (2013) method. Targeted tracer release experiments (both numerical and real) similar to what has been described in Sec. V C also present a useful tool for identifying invariant surfaces in time-dependent flows. A comparison between all of the methods would be valuable, and the results from our kinematic model provide a standard.

Visualization of time-varying boundaries is important, not only for intuition building but also for experimental tracer releases, which may be the only viable technique for observing such structures in the ocean and demonstrating that they can withstand the diffusive effects of background turbulence. Without a three-dimensional visualization, it can be difficult to form a mental picture of many of the colored surfaces shown in the lower panels of Fig. 5. It is unlikely that these will become any simpler if the time dependence

becomes aperiodic. This is perhaps an opportunity for collaborations between artists and scientists (e.g., Osinga and Krauskopf (2004)).

Although azimuthal swirling and vertical overturning arising in the rotating can flow are essential elements of many observed oceanic eddies, our model is highly idealized and thus only represents a first step towards establishing the utility of the dynamical systems approach to real oceanic flows. In addition to non-periodic forcing, future work could consider the effects of stratification, as well as fluid exchange between the eddy interior and the surrounding fluid through, for example, relaxing the limitation the limitation that the flow is contained within rigid vertical walls.

ACKNOWLEDGMENTS

This work has been supported on DOD (MURI) Grant No. N000141110087, administered by the Office of Naval Research.

APPENDIX A: MULTI-SCALE ANALYSIS OF DEGENERATE RESONANCES

We are interested in investigating the behavior of trajectories close to a degenerate resonant torus I_0 satisfying $n\Omega_\phi(I_0)+n\Omega_\theta(I_0)-\vec{l}\cdot\vec{\sigma}=0$, $\frac{d^j(n\Omega_\phi+m\Omega_\theta)}{dI^j}\Big|_{I_0}\neq 0$, $\frac{d^i(n\Omega_\phi+m\Omega_\theta)}{dI^i}\Big|_{I_0}=0$ for $i<j$. Scaling arguments described in Sec. III B suggest that δI will grow to $O(\epsilon^{1/(j+1)})$ over $t\sim O(\epsilon^{-j/(j+1)})$. We therefore define the generalyzed slow time variable $\tau=\epsilon^{j/(j+1)}t$ and treat t and τ as two independent variables leading to $d/dt=\partial/\partial t+\epsilon^{j/(j+1)}\partial/\partial\tau$. The previously considered non-degenerate case is represented by $j=1$.

It is convenient to introduce a phase variable $\eta_{nml\vec{l}}=n\phi+m\theta-\vec{l}\cdot\vec{\sigma}t+\alpha_{nml\vec{l}}$, whose evolution, according to (3), is governed by

$$\frac{d\eta}{dt}=n\Omega_\phi(I)+m\Omega_\theta(I)-\vec{l}\cdot\vec{\sigma}+\epsilon\left[nF^1(I,\phi,\theta,\vec{\sigma}t)+mF^2(I,\phi,\theta,\vec{\sigma}t)\right]. \tag{A1}$$

We then write down the multi-scale expansions for δI and $\eta_{nml\vec{l}}$ as

$$\delta I=\epsilon^{\frac{1}{j+1}}\delta I_0(t,\tau)+\epsilon^{\frac{2}{j+1}}\delta I_1(t,\tau)+\cdots+\epsilon\delta I_j(t,\tau)+\cdots$$
$$\eta_{nml\vec{l}}=\eta_{0,nml\vec{l}}(t,\tau)+\epsilon^{\frac{1}{j+1}}\eta_{1,nml\vec{l}}(t,\tau)+\cdots\epsilon\eta_{j+1,nml\vec{l}}(t,\tau)+\cdots.$$

Substituting these expansions into (A1) and the first equation in (3), and using the Fourier decomposition for the perturbation (4), we obtain

$$\begin{aligned}&\frac{\partial}{\partial t}\left[\epsilon^{\frac{1}{j+1}}\delta I_0(t,\tau)+\epsilon^{\frac{2}{j+1}}\delta I_1(t,\tau)+\cdots+\epsilon\delta I_j(t,\tau)+\cdots\right]\\&+\epsilon^{\frac{j}{j+1}}\frac{\partial}{\partial\tau}\left[\epsilon^{\frac{1}{j+1}}\delta I_0(t,\tau)+\epsilon^{\frac{2}{j+1}}\delta I_1(t,\tau)+\cdots+\epsilon\delta I_j(t,\tau)+\cdots\right]\\&=\epsilon\sum_{nml\vec{l}}F^0_{nml\vec{l}}(I_0+\delta I)\sin\left[\eta_{0,nml\vec{l}}(t,\tau)+\epsilon^{\frac{1}{j+1}}\eta_{1,nml\vec{l}}(t,\tau)+\cdots\right]\end{aligned} \tag{A2}$$

and

$$\begin{aligned}&\frac{\partial}{\partial t}\left[\eta_{0,nml\vec{l}}(t,\tau)+\epsilon^{\frac{1}{j+1}}\eta_{1,nml\vec{l}}(t,\tau)+\cdots\right]\\&+\epsilon^{\frac{j}{j+1}}\frac{\partial}{\partial\tau}\left[\eta_{0,nml\vec{l}}(t,\tau)+\epsilon^{\frac{1}{j+1}}\eta_{1,nml\vec{l}}(t,\tau)+\cdots\right]\\&=n\Omega_\phi(I_0)+m\Omega_\theta(I_0)-\vec{l}\cdot\vec{\sigma}+\frac{d^j(n\Omega_\phi+m\Omega_\theta)}{dI^j}\Big|_{I_0}\\&\times\frac{\left(\epsilon^{\frac{1}{j+1}}\delta I_0(t,\tau)+\epsilon^{\frac{2}{j+1}}\delta I_1(t,\tau)+\cdots\right)^j}{j!}\\&+\epsilon\sum_{nml\vec{l}}\left[nF^1_{nml\vec{l}}(I_0+\delta I)+mF^2_{nml\vec{l}}(I_0+\delta I)\right]\\&\times\sin\left[\eta_{0,nml\vec{l}}(t,\tau)+\epsilon^{\frac{1}{j+1}}\eta_{1,nml\vec{l}}(t,\tau)+\cdots\right].\end{aligned} \tag{A3}$$

Combining the leading order $O(\epsilon^{1/(j+1)})$ terms in Eq. (A2) and $O(1)$ terms in Eq. (A3) yields to

$$\delta I_0=\delta\tilde{I}_0(\tau), \tag{A4}$$

$$\eta_{0,nml\vec{l}}=[n\Omega_\phi(I_0)+m\Omega_\theta(I_0)-\vec{l}\cdot\vec{\sigma}]t+\tilde{\eta}_{nml\vec{l}}(\tau). \tag{A5}$$

To find the slowly-varying functions $\delta\tilde{I}_0(\tau)$ and $\tilde{\eta}_{nml\vec{l}}(\tau)$, we examine the $O(\epsilon)$ balance in (A2) along with the $O(\epsilon^{j/(j+1)})$ balance in (A3)

$$\frac{\partial}{\partial t}\delta I_j=-\frac{\partial}{\partial\tau}\delta\tilde{I}_0+\sum_{nml\vec{l}}F^0_{nml\vec{l}}(I_0)\sin\left[\tilde{\eta}_{nml\vec{l}}(\tau)+(n\Omega_\phi(I_0)+m\Omega_\theta(I_0)-\vec{l}\cdot\vec{\sigma})t\right] \tag{A6}$$

and

$$\frac{\partial}{\partial t}\eta_{j,nml\vec{l}}=-\frac{\partial}{\partial\tau}\tilde{\eta}_{nml\vec{l}}(\tau)+\frac{d^j(n\Omega_\phi+m\Omega_\theta)}{dI^j}\Big|_{I_0}\frac{\delta\tilde{I}_0{}^j}{j!}. \tag{A7}$$

Elimination of terms leading to secular growth of δI_j and $\eta_{j,nml\vec{l}}$ gives

$$\frac{\partial}{\partial\tau}\delta\tilde{I}_0=\sum_{nml\vec{l}}^{resonant}F^0_{nml\vec{l}}(I_0)\sin\left[\tilde{\eta}_{nml\vec{l}}(\tau)\right] \tag{A8}$$

and

$$\frac{\partial}{\partial\tau}\tilde{\eta}_{nml\vec{l}}=\frac{d^j(n\Omega_\phi+m\Omega_\theta)}{dI^j}\Big|_{I_0}\frac{\delta\tilde{I}_0{}^j}{j!}. \tag{A9}$$

The last two equations admit the integral of motion

$$G=\frac{\delta\tilde{I}_0^{j+1}}{(j+1)!}+\sum_{nml\vec{l}}^{resonant}\frac{F^0_{nml\vec{l}}(I_0)\cos\tilde{\eta}_{nml\vec{l}}}{\frac{d^j(n\Omega_\phi+m\Omega_\theta)}{dI_j}\Big|_{I_0}}. \tag{A10}$$

Beron-Vera, F. J., Wang, Y., Olascoaga, M. J., Goni, J. G., and G. Haller, "Objective detection of oceanic eddies and the Agulhas leakage," J. Phys. Oceanogr. **43**, 1426–1438 (2013).

Budisic, M. and Mezic, I., "Geometry of the ergodic quotient reveals coherent structures in flows," Physica D **241**, 1255–1269 (2012).

Cartwright, J. H. E., Feingold, M., and Piro, O., "Global diffusion in a realistic three-dimensional time-dependent nonturbulent fluid flow," Phys. Rev. Lett. **75**, 3669–3672 (1995).
Cartwright, J. H. E., Feingold, M., and Piro, O., "Chaotic advection in three dimensional unsteady incompressible laminar flow," J. Fluid Mech. **316**, 259–284 (1996).
Cheng, C.-Q. and Sun, Y.-S., "Existence of invariant tori in three-dimensional measure-preserving mappings," Celestial Mech. **47**, 275–292 (1990).
Chirikov, B. V., "A universal instability of many-dimensional oscillator systems," Phys. Rep. **52**, 263–379 (1979).
Dullin, H. R. and Meiss, J. D., "Resonances and twist in volume-preserving mappings," Siam J. Appl. Dyn. Syst. **11**, 319–349 (2012).
Fischer, P. F., "An overlapping schwarz method for spectral element solution of the incompressible Navier-Stokes equations," J. Comput. Phys. **133**, 84–101 (1997).
Fountain, G. O., Khakhar, K. V., Mezic, I., and Ottino, J. M., "Chaotic mixing in a bounded three-dimensional flow," J. Fluid Mech. **417**, 265–301 (2000).
Fox, A. M. and Meiss, J. D., "Greene's residue criterion for the breakup of invariant tori of volume-preserving maps," Physica D **243**(1), 45–63 (2013).
Froyland, G., Padberg, K., England, M. H., and Treguier, A. M., "Detection of coherent oceanic structures via transfer operators," Phys. Rev. Lett. **98**, 224503 (2007).
Greenspan, H. P., *The Theory of Rotating Fluids* (Cambridge University Press, 1968).
Lackey, T. C. and Sotiropoulos, F., "Relationship between stirring rate and Reynolds number in the chaotically advected steady flow in a container with exactly counter-rotating lids," Phys. Fluids **18**(5), 053601 (2006).
Ledwell, J. R., McGillicuddy, D. J., and Anderson, L. A., "Nutrient flux into an intense deep chlorophyll layer in a mode-water eddy," Deep Sea Res., Part II **55**, 1139–1160 (2008).
Lomeli, H. E. and Ramirez-Ros, R., "Separatrix splitting in 3d volume-preserving maps," SIAM J. Appl. Dyn. Syst. **7**(4), 1527–1557 (2008).
Lopez, J. M. and Marques, F., "Sidewall boundary layer instabilities in a rapidly rotating cylinder driven by a differentially co-rotating lid," Phys. Fluids **22**, 114109 (2010).
Maday, Y. and Patera, A. T., "Spectral element methods for the Navier-Stokes equations," *State of the Art Surveys in Computational Mechanics* (ASME, 1989), pp. 71–143.
Maslowe, S. A. and Clarke, S. R., "Subcritical Rossby waves in zonal shear flows with nonlinear critical layers," Stud. Appl. Math. **108**, 89–103 (2002).
McGillicuddy, D. J., *et al.*, "Eddy/wind interactions stimulate extraordinary mid-ocean plankton blooms," Science **316**(5827), 1021–1026 (2007).
Meiss, J. D., "The destruction of tori in volume-preserving maps," Commun. Nonlinear Sci. Numer. Simul. **17**, 2108–2121 (2012).
Mendoza, C., Mancho, A. M., and Wiggins, S., "Lagrangian descriptors and the assessment of the predictive capacity of oceanic data sets," Nonlinear Process. Geophys. **21**, 677–689 (2014).
Mezic, I. and Sotiropoulos, F., "Ergodic theory and experimental visualization of invariant sets in chaotically advected flows," Phys. Fluids **14**(7), 2235–2243 (2002).
Mezic, I. and Wiggins, S., "On the integrability of perturbations of three-dimensional fluid flows with symmetry," J. Nonlinear Sci. **4**, 157–194 (1994).
Mireles-James, J. D. and Lomeli, H. E., "Computation of heteroclinic arcs with application to the volume preserving Henon family," SIAM J. Appl. Dyn. Syst. **9**(3), 919–953 (2010).
Moharana, N. R., Speetjens, M. F. M., Trieling, R. R., and Clercx, H. J. H., "Three-dimensional Lagrangian transport phenomena in unsteady laminar flows driven by a rotating sphere," Phys. Fluids **25**, 093602 (2013).
Osinga, H. M. and Krauskopf, B., "Crocheting the Lorenz manifold," Math. Intell. **26**(4), 25–37 (2004).
Patera, A., "A spectral element method for fluid dynamics; laminar flow in a channel expansion," J. Comput. Phys. **54**, 468–488 (1984).
Pouransari, Z., Speetjens, M. F. M., and Clercx, H. J. H., "Formation of coherent structures by fluid inertia in three-dimensional laminar flows," J. Fluid Mech. **654**, 5–34 (2010).
Pratt, L. J., Rypina, I. I., Özgökmen, T. M., Wang, P., Childs, H., and Bebieva, Y., "Chaotic advection in a steady, three-dimensional, ekman-driven eddy," J. Fluid Mech. **738**, 143–183 (2014).
Rom-Kedar, V., Kadanoff, L. P., Ching, E. S. C., and Amick, C., "The break-up of a heteroclinic connection in a volume preserving mapping," Physica D **62**, 51–65 (1993).
Rypina, I. I., Brown, M. G., Beron-Vera, F. J., Kocak, H., Olascoaga, M. J., and Udovydchenkov, I. A., "On the Lagrangian dynamics of atmospheric zonal jets and the permeability of the Stratospheric Polar Vortex," J. Atmos. Sci. **64**, 3595–3610 (2007a).
Rypina, I. I., Brown, M. G., Beron-Vera, F. J., Kocak, H., Olascoaga, M. J., and Udovydchenkov, I. A., "Robust transport barriers resulting from strong Kolmogorov-Arnold-Moser stability," Phys. Rev. Lett. **98**, 104102 (2007b).
Rypina, I. I., Pratt, L. J., Pullen, J., Levin, J., and Gordon, A., "Chaotic advection in an archipelago," J. Phys. Oceanogr. **40**(9), 1988–2006 (2010).
Rypina, I. I., Scott, S. E., Pratt, L. J., and Brown, M. G., "Investigating the connection between complexity of isolated trajectories and lagrangian coherent structures," Nonlinear Proc. Geophys. **18**, 977–987 (2011).
Samelson, R. M. and Wiggins, S., *Lagrangian Transport in Geophysical Jets and Waves: The Dynamical Systems Approach* (Springer-Verlag, New York, LLC, 2006).
Solomon, T. H. and Mezic, I., "Uniform resonant chaotic mixing in fluid flows," Nature **425**, 376–380 (2003).
Speetjens, M. F. M. and Clercx, H. J. H., "A spectral solver for the Navier-Stokes equations in the velocity-vorticity formulation," Int. J. Comput. Fluid Dyn. **19**(3), 191–209 (2005).
Vainchtein, D. L., Widloski, J., and Grigoriev, R. O., "Resonance phenomena and chaotic advection in a cellular flow," Phys. Rev. Lett. **99**, 094501 (2007).
Vainchtein, D. L., Widloski, J., and Grigoriev, R. O., "Resonant chaotic mixing in a cellular flow," Phys. Rev. E **78**, 026302 (2008).
Xia, Z., "Existence of invariant tori in volume-preserving diffeomorphisms," Ergodic Theor. Dyn. Syst. **12**, 621–631 (1992).
Zaslavsky, G., *Chaos in Dynamic Systems* (Harwood Academic Publishers, NY, 1985).
Zaslavsky, G. M. and Chirikov, B. V., "Stochastic instability of non-linear oscillations," Sov. Phys. Usp. **14**, 549–672 (1972).
Znaien, J., Speetjens, M. F. M., Trieling, R. R., and Clercx, H. J. H., "Observability of periodic lines in three-dimensional lid-driven cylindrical cavity flows," Phys. Rev. E **85**, 066320 (2012).